

Uncovering the ultimate planet impostor[★]

An eclipsing brown dwarf in a hierarchical triple with two evolved stars

J. Lillo-Box¹, Á. Ribas², B. Montesinos¹, N. C. Santos^{3,4}, T. Campante^{3,4}, M. Cunha³, D. Barrado¹,
E. Villaver¹, S. Sousa³, H. Bouy⁵, A. Aller^{1,6}, E. Corsaro⁷, T. Li^{8,9}, J. M. J. Ong¹⁰,
I. Rebollido¹¹, J. Audenaert¹², F. Pereira³

¹ Centro de Astrobiología (CAB, CSIC-INTA), Depto. de Astrofísica, ESAC campus 28692 Villanueva de la Cañada (Madrid), Spain e-mail: Jorge.Lillo@cab.inta-csic.es

² European Southern Observatory, Alonso de Cordova 3107, Vitacura, Region Metropolitana, Chile

³ Instituto de Astrofísica e Ciências do Espaço, Universidade do Porto, CAUP, Rua das Estrelas, PT4150-762 Porto, Portugal

⁴ Depto. de Física e Astronomia, Faculdade de Ciências, Universidade do Porto, Rua do Campo Alegre, 4169-007 Porto, Portugal

⁵ Laboratoire d'astrophysique de Bordeaux, Univ. Bordeaux, CNRS, B18N, allée Geoffroy Saint-Hilaire, 33615 Pessac, France

⁶ Spanish Virtual Observatory, Spain

⁷ INAF – Osservatorio Astrofisico di Catania, Via S. Sofia 78, 95123 Catania, Italy

⁸ School of Physics and Astronomy, University of Birmingham, Edgbaston, B15 2TT, UK

⁹ Stellar Astrophysics Centre, Department of Physics and Astronomy, Aarhus University, 8000 Aarhus C, Denmark

¹⁰ Department of Astronomy, Yale University, 52 Hillhouse Ave., New Haven, CT 06511, USA

¹¹ Space Telescope Science Institute, 3700 San Martin Drive, Baltimore, MD 21218, USA

¹² Institute of Astronomy, KU Leuven, Celestijnenlaan 200D, BUS-2410, Belgium

in prep

ABSTRACT

Context. Exoplanet searches through space-based photometric time series have shown to be very efficient in recent years. However, follow-up efforts on the detected planet candidates have been demonstrated to be critical to uncover the true nature of the transiting objects.

Aims. In this paper we show a detailed analysis of one of those false positives hidden as planetary signals. In this case, the candidate KOI-3886.01 showed clear evidence of a planetary nature from various techniques. Indeed, the properties of the fake planet set it among the most interesting and promising for the study of planetary evolution as the star leaves the main sequence.

Methods. To unveil the true nature of this system, we present a complete set of observational techniques including high-spatial resolution imaging, high-precision photometric time series (showing eclipses, phase curve variations, and asteroseismology signals), high-resolution spectroscopy, and derived radial velocities to unveil the true nature of this planet candidate.

Results. We find that KOI-3886.01 is an interesting false positive case: a hierarchical triple system composed by a \sim K2 III giant star (KOI-3886 A) accompanied by a close-in eclipsing binary formed by a subgiant \sim G4 IV star (KOI-3886 B) and a brown dwarf (KOI-3886 C). In particular, KOI-3886 C is one of the most irradiated brown dwarfs known to date, showing the largest radius in this substellar regime. It is also the first eclipsing brown dwarf known around an evolved star.

Conclusions. In this paper we highlight the relevance of complete sets of follow-up observations to extrasolar planets detected by the transit technique using large-pixel photometers such as *Kepler* and TESS and, in the future, PLATO. In particular, multi-color high-spatial resolution imaging was the first hint toward ruling out the planet scenario in this system.

Key words. (Stars:) binaries: eclipsing, brown dwarfs, close – Stars: oscillations

1. Introduction

The complex process of detecting extrasolar planet candidates and validating their true planetary nature has been refined during recent years of exoplanet exploration. The launch of the *Kepler* mission (Borucki et al. 2010) and the many planet-like signals detected in its first months of operations made it necessary to come up with dedicated follow-up observing programs perform-

ing specific observations to rule out other possible configurations mimicking a planet-like transit signal. Specifically, high-spatial resolution images became a key starting point in this validation process (Howell et al. 2011; Law et al. 2014; Lillo-Box et al. 2012, 2014b; Furlan et al. 2017). Given the large pixel size of the *Kepler* CCD (4×4 arcsec) and now even more importantly in the Transiting Exoplanet Survey Satellite (TESS; Ricker et al. 2014) photometer (21×21 arcsec), understanding and measuring the flux contamination from both chance-aligned and bound sources are essential to validate planet candidates (especially the smallest planets, e.g., Barclay et al. 2013) and to refine their physical and orbital parameters (Lillo-Box et al. 2014b). A second step in this process is the radial velocity (RV) monitoring of the host candidate to detect the amplitude and shape of the modula-

[★] Based on observations collected at Centro Astronómico Hispano en Andalucía (CAHA) at Calar Alto, operated jointly by Instituto de Astrofísica de Andalucía (CSIC) and Junta de Andalucía and observations made with the Mercator Telescope, operated on the island of La Palma by the Flemish Community, at the Spanish Observatorio del Roque de los Muchachos of the Instituto de Astrofísica de Canarias.

tions to infer a mass for the transiting companion. Although this is not always possible given the low planetary masses (e.g., in the rocky regime, [Barclay et al. 2013](#)), high-resolution spectra can be used to provide upper limits to their masses and to discard additional scenarios undetectable by the high-spatial resolution images (e.g., close bound binaries) through analysis of the cross-correlation function (hereafter CCF). This proved to be especially relevant in some specific cases of planet-like signals that were subsequently uncovered to be of stellar or substellar nature (e.g., [Santos et al. 2002](#)). All this experience from exoplanet detection and follow-up efforts puts on the table the need for dedicated observations after transit measurements.

In this work we describe a new example of an impostor planet. The KOI-3886 system showed all apparent signs of being a truly high-impact discovery with a potential gigantic planet around an evolved red giant branch (RGB) star skimming the Roche Lobe overflow point. This gigantic planet would have had an expected remaining lifetime of below five million years - a really lucky catch of the last breath of a monster planet. In this paper, we show evidence that leads to disguising KOI-3886.01 as a planet candidate in favor of a complex hierarchical triple system composed by a \sim K2 III star ascending the RGB orbited by an evolved \sim G4 IV subgiant star at a projected distance of 270 au, the latter surrounded by an eclipsing inflated brown dwarf in a very close-in orbital period of 5.6 days.

Brown dwarfs are substellar objects that do not have enough mass to trigger the burning of hydrogen in their nuclei. Theoretical models for their formation and evolutionary structure (i.e., mass, radius, luminosity) are difficult to calibrate given the very low number of brown dwarfs that have been fully characterized (i.e., have had their mass, radius, and age measured). To retrieve the size of these bodies and thus feed these evolutionary models, detecting eclipsing brown dwarfs is critical. So far, to our knowledge, only 26 eclipsing brown dwarfs have been detected (see [Carmichael et al. 2020a](#) and references therein, as well as the latest discoveries by [Jackman et al. 2019a](#); [Šubjak et al. 2020](#); [Palle et al. 2021](#)). Most of these eclipsing brown dwarfs are orbiting mature main-sequence stars of different spectral types, whose ages are difficult to determine using traditional isochrone fitting approach. Theoretical studies suggest that these substellar objects present large radii during the first stages of their formation while they are contracting to reach Jupiter-like (or even smaller) sizes. The very few eclipsing brown dwarfs detected around young stars (e.g., [Stassun et al. 2006a](#)) show radii larger than the theoretical values, thereby pointing to this scenario. However, more mature eclipsing brown dwarfs also show radii larger than the expected by theoretical predictions. This can be attributed to stellar irradiation ([Hernández Santisteban et al. 2016](#)) by the companion. However, the lack of precise age measurements also prevents a direct comparison with models. The KOI-3886 system offers an excellent environment in which the presence of a RGB star presenting solar-like oscillations allows a precise measurement of the age of the system. This measurement, together with the eclipsing nature of the brown dwarf, allows for a full characterization of its properties. Hence, KOI-3886 is a benchmark system for the study of brown dwarf properties in a hostile environment.

Interestingly, the subgiant nature of the host star and the mass of the eclipsing object enhance the presence of the well-known reflexion, ellipsoidal, and beaming light curve modulations, which have recently been used to confirm (i.e., obtain the mass of) new planets (e.g., [Lillo-Box et al. 2014a](#); [Millholland & Laughlin 2017](#); [Lillo-Box et al. 2021](#)) and substellar objects

Table 1. General properties of the KOI-3886 system.

Parameter	Value	Ref. [†]
IDs	KOI-3886, HD 190655, KIC 8848288, TIC 185060864	
Gaia EDR3 ID	2082133182277361152	[1]
RA, DEC	20:04:11.33, +45:05:15.30	[1]
Parallax (mas)	2.14 ± 0.30	[1]
μ_α (mas/yr)	-8.41 ± 0.37	[1]
μ_δ (mas/yr)	-3.18 ± 0.37	[1]
RV (km/s)	-24.00 ± 0.64	[1]
G (mag)	10.1	[1]
$B_p - R_p$ (mag)	1.28	[1]
m_V (mag)	10.306 ± 0.050	[2]
Ks (mag)	7.475 ± 0.023	[3]
U (km/s)	-3.955	[4]
V (km/s)	-23.478	[4]
W (km/s)	-3.026	[4]
Gal. population	Thin disk	[4]

References. [1] Gaia Collaboration et al. (2016); [2] Bessell et al. (1998); [3] Cohen et al. (2003); [4] This work.

(e.g., [Mazeh et al. 2012](#); [Lillo-Box et al. 2016](#)) directly from a light curve as an alternative to RV monitoring.

The paper is organized as follows: in Sect. 2 we present the observations that lead to unveiling the nature of the KOI-3886 system; we then show evidence against the planetary nature of the eclipsing candidate in Sect. 3. In Sect. 4 we use all the observations to fully characterize the system. We discuss the results in Sect. 5 and conclude in Sect. 6.

2. Observations

2.1. Kepler and TESS photometric time series

KOI-3886 (HD190655, KIC 8848288, TIC 185060864, see Table 1) was observed by the *Kepler* mission ([Borucki et al. 2010](#)) between 2010 and 2014 in long-cadence mode, obtaining one photometric measurement every 30 minutes. The TESS mission also observed this target as part of its 2 min cadence legacy in Sector 14 during 27.4 days. Figure 1 shows the median target pixel file (TPF) from this TESS observation (computed using `tpfplotter`; [Aller et al. 2020](#)). The figure shows no contaminant sources within the aperture detected by Gaia DR2 down to 8 magnitudes contrast against the Gaia magnitude of the target. The same applies to the *Kepler* aperture.

We obtained the *Kepler* and TESS light curves from the MAST archive¹ and used the PDCSAP (Pre-Data Conditioned Search Aperture Photometry) flux for our analysis. The periodogram of the *Kepler* light curve shows evidence for a modulation at 5.56 days, corresponding to the transiting candidate planet KOI-3886.01 reported by the *Kepler* team ([Batalha et al. 2013](#)). In Fig. 2, we show the combination of chunks of 10 orbits per line in the region around the detected eclipse signal. In total, more than 260 orbits are available in the *Kepler* data. When phase-folding the light curve with such periodicity we noticed

¹ <https://mast.stsci.edu/portal/Mashup/Clients/Mast/Portal.html>

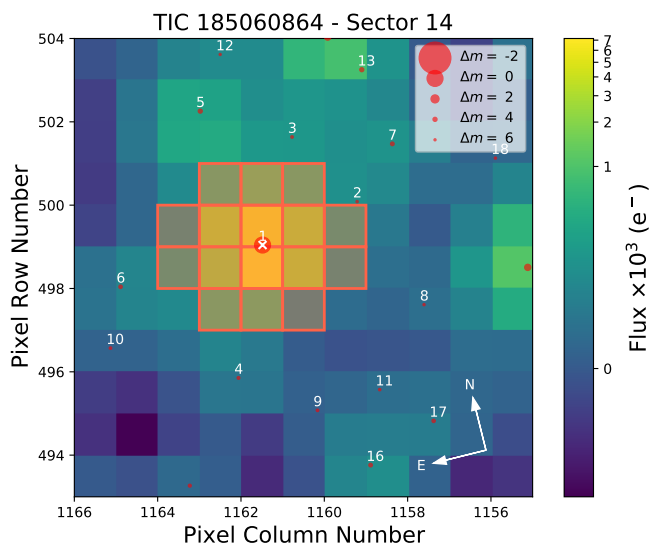


Fig. 1. Target pixel file of KOI-3886 obtained with *tpfplotter* (Aller et al. 2020) from Sector 14 of the TESS mission.

two clear signals: the transit dimming and a clear double hump in the out-of-transit region (see Fig. 3). The transit signal has a depth of about 700 ppm (parts per million). The out-of-eclipse modulations indicate the presence of ellipsoidal variations due to tidal interaction between the star and the transiting object. The amplitude of these modulations is at the level of 200 ppm.

The periodogram also shows a clear forest of power frequencies around $50 \mu\text{Hz}$ (see Fig. 4), corresponding to typical solar-like oscillations of a red giant star (as shown for instance in the case of the confirmed planet host Kepler-91; see Lillo-Box et al. 2014a). This is analysed in depth in Sect. 4.3.

The *Kepler* Data Validation Report (DVR) indicates large excursions of the out of transit centroids (> 3 arcsec from the target position). However, these are probably caused by the large amplitudes of the asteroseismology oscillations, implying flux variations of up to 1 part per thousand (ppt).

Given the largely shorter temporal coverage of the TESS data set against the *Kepler* data (27.8 days versus 1400 days) and the presence of the above described stellar oscillations, which make it necessary to combine a large set of orbits to average out this effect, we decided to not use the TESS dataset further for the sake of simplicity in this paper.

2.2. High-spatial resolution imaging

In Lillo-Box et al. (2014b), we presented a high-spatial resolution image of KOI-3886 obtained through the lucky imaging technique with the AstraLux North instrument (Hormuth et al. 2008) located at the 2.2 m telescope at the Calar Alto Observatory (Almeria, Spain). The image (see Fig. 5) showed a very close companion (hereafter called KOI-3886 B) located at 0.43 arcsec to the brightest object (KOI-3886 A) and with a magnitude contrast of 0.85 mag in the i' band (0.99 mag in the z' band). Additionally, images from Robo-AO (Ziegler et al. 2017) and PHARO (Furlan et al. 2017) were also published in the literature. Both high-resolution images also detected this close companion with a magnitude contrast of 2.2 mag in the K band. Based on these contrast magnitudes we can estimate a dilution factor of 43% in the *Kepler* band, assuming the eclipses occur in the brighter companion. This is a significant source of contamination, which needs to be taken into account in the modeling of the

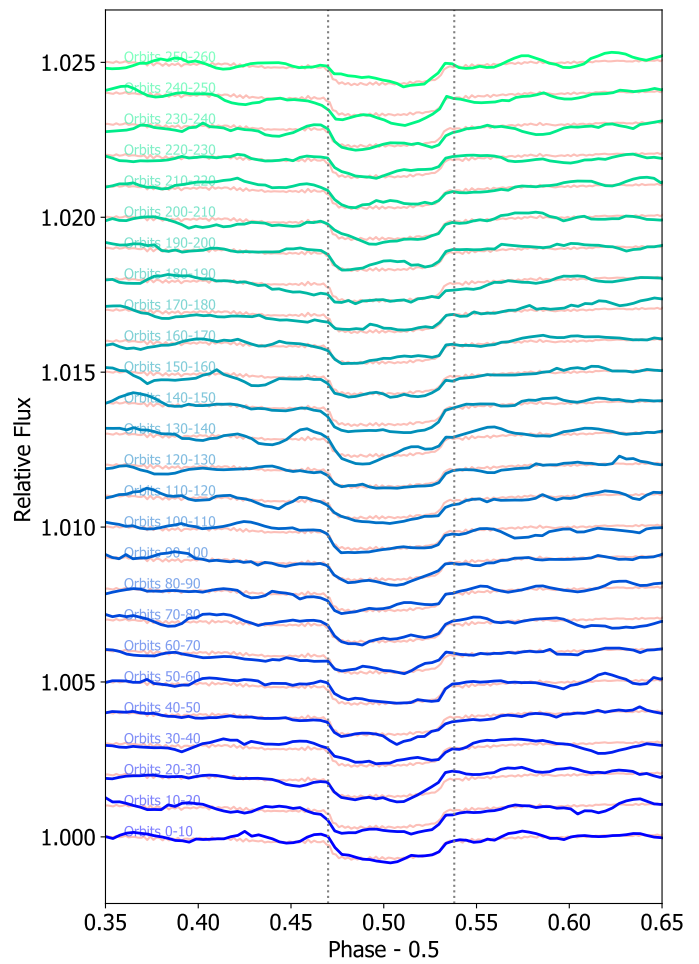


Fig. 2. Phase-folded *Kepler* light curve centered in the mid-eclipse. Each line includes a combination of 10 orbits. The asteroseismology signal from KOI-3886 A is mixed with the eclipse signal at a similar flux variation level. The full combined light curve is shown for reference on each chunk.

light curve. It also brings up the question of which is the host of the eclipsing object. If star B is the host, the dilution factor becomes 71%.

2.3. Spectral energy distribution

Table A.1 shows the observed photometry of KOI-3886. Among the large amount of observations available, we carried out a careful and critical selection of the magnitudes, therefore the values listed in the table can be considered as a clean set of data. Sources of fluxes at zero magnitude are as follows: Tycho BV (Mann & von Braun 2015), Johnson UBV (Bessell et al. 1998), and 2MASS JHK_s (Cohen et al. 2003). The GALEX NUV (Olmedo et al. 2015) and Sloan magnitudes $g'r'i'z'$ (Fukugita et al. 1996; York et al. 2000) are on the AB system, thus a flux of 3631 Jy was adopted in both cases. Regarding the GALEX NUV flux, which plays an important role in the spectral energy distribution (SED), discrepancies between the filter effective wavelength are found in the literature. The value of the GALEX NUV flux affects the conversion of the fluxes in Jy, computed from the AB magnitude, to cgs units used in this work; in this work we

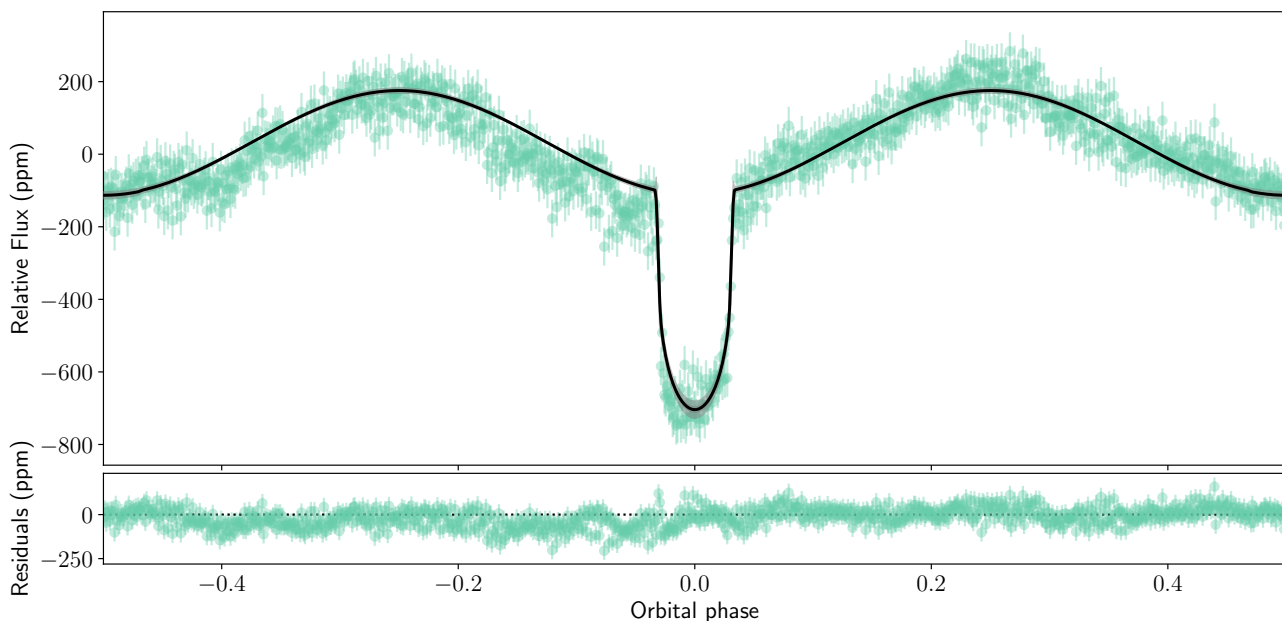


Fig. 3. Diluted *Kepler* light curve phase folded with the eclipse period and the inferred median model from the joint analysis from Sect. 4.5. The corresponding 95% confidence interval is shown as a vgray shaded region. *Kepler* data has been binned in phase to remove the asteroseismology variation due to the contaminant bright KOI-3886 A star.

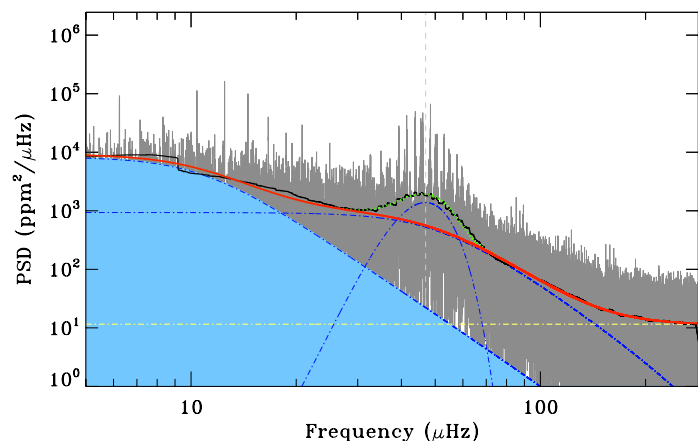


Fig. 4. Power spectrum of KOI-3886. The power spectrum is shown in gray (with a heavily smoothed version in black). The solid red curve indicates a fit to the background done with DIAMONDS (Corsaro & De Ridder 2014), consisting of two Harvey-like profiles (dot-dashed blue curves) plus white noise (horizontal dot-dashed yellow line). A joint fit to the oscillation power excess (dot-dashed blue Gaussian curve) and background is visible at $\sim 50 \mu\text{Hz}$ as a dotted green curve.

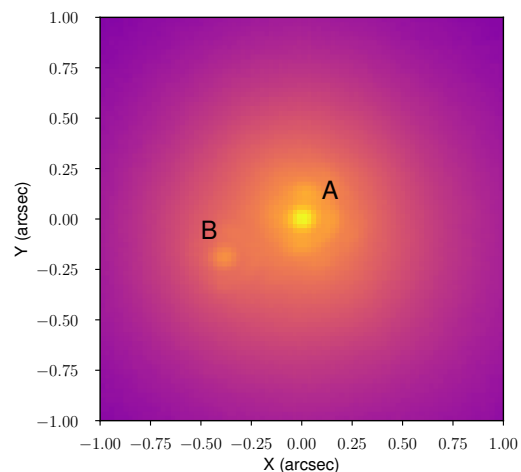


Fig. 5. AstraLux image of the KOI-3886 system.

adopted the value 2315.7 \AA from Beitia-Antero & Gómez de Castro (2016).

The observed SED is shown in Fig. 6 as empty black circles. A one-component temperature fit, plotted as red crosses and a pale red line, shows that whereas the photometry at optical ($\lambda > 5000 \text{ \AA}$) and near-infrared wavelengths is well reproduced, an additional hotter component, not modifying the shape of the final, composite fit at these wavelengths, but accounting for the deficit of fluxes at bluer wavelengths, and especially for the NUV GALEX point, is required. This clearly suggests that the brightest component (KOI-3886 A), which dominates the region above $\sim 5000 \text{ \AA}$, must be colder than the fainter component (KOI-3886 B). This is very relevant to unveil the architec-

ture of this system. The composite fit to this SED is shown in Sect. 4.4.1.

2.4. High-resolution spectroscopy and preliminary radial velocities

We observed KOI-3886 using the fiber-fed high-resolution spectrograph HERMES (Raskin et al. 2011) located at the 1.2 m Mercator telescope at the Roque de los Muchachos Observatory (La Palma, Spain). The observations were carried out during five consecutive nights on 15-19 July 2020 in visitor mode and another five epochs within a week time span between 22-29 July 2020. We used the simultaneous reference observing mode, in which the second fiber is illuminated by ThAr and Ne lamps, which imprints the emission lines from these species in the inter-order region of fiber B. This strategy allows us to

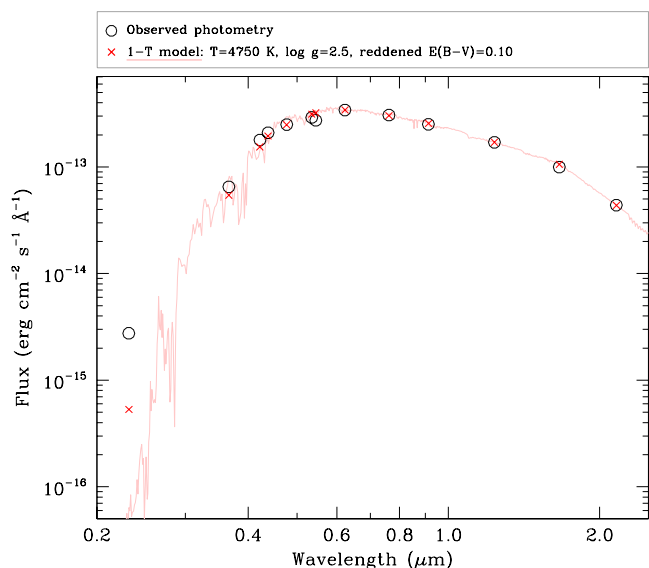


Fig. 6. Observed photometry of KOI-3886 (empty black circles), and a 1T-model fit of a Kurucz model (Kurucz 1979) with $T_{\text{eff}}=4750$ K and $\log g_{*}=2.5$ (red crosses and solid pale red line). Whereas the red part of the SED is well reproduced by the model, the fluxes below ~ 5000 Å, and in particular that corresponding to the NUV GALEX band, are underestimated.

keep track of intra-night RV drifts at the 2 m/s level. Added to this, we observed the RV standard HD 109358 ($V=4.25$ mag) to measure possible night-to-night offsets since the instrument is not pressure-stabilized (only the temperature is actively controlled). Among the five nights, the third was performed under poor weather conditions with high clouds interrupting the observations. Hence, the data from that night are of less quality. We obtained three spectra per night on the first run and one spectrum per night on the second run. The typical signal-to-noise ratio (S/N) of the dataset is 20. The data were reduced by using the standard pipeline of the instrument. We first extracted the RV through cross-correlating the spectra with a binary mask constructed from a solar-like spectrum. We measured the nightly offsets by using the RVs of the standard star. This nightly offsets were then subtracted from the target RVs. The median precision on the RVs is 5.6 m/s.

High-resolution spectra of KOI-3886 were also obtained with the CAFE fiber-fed spectrograph (Aceituno et al. 2013; Lillo-Box et al. 2020) installed at the coudé room of the 2.2 m telescope of the Calar Alto Observatory (Almería, Spain). The system was observed on the nights of 23-24 of July 2020, together with the RV standard HD 109358 to measure inter-night RV offsets since the instrument is not pressure-controlled. Additionally, we obtained ThAr reference frames before and after each science image to measure the intra-night drift. The conditions on both nights were optimal with a typical seeing of 1 arcsec. We obtained 18 spectra of KOI-3886 (three per night spread along the whole night) with a mean S/N of 30. We reduced the spectra using the instrument pipeline *cafextractor* (Lillo-Box et al. 2020). Besides the basic reduction and the wavelength calibration, *cafextractor* measures the RV of each spectrum by cross-correlating them with a G2 mask custom-made for the in-

strument. The pipeline uses the drift measurement to correct this RV. Additionally, we remove the offset corresponding to the RV standard as measured at the beginning of the night. The final median photon noise of the RVs corresponds to ~ 10 m/s.

2.5. Gaia

We checked the KOI-3886 system on the Gaia EDR3 catalog (Lindgren et al. 2021). Although this target was not reported in the second Gaia release (DR2), the EDR3 release now includes this target (Gaia EDR3 2082133182277361152). The catalog provides a parallax of $\pi = 2.13 \pm 0.31$ mas and proper motions of $\mu_{\alpha} = -8.41 \pm 0.37$ mas/yr, $\mu_{\delta} = -3.17 \pm 0.37$ mas/yr (see Table 1). The corresponding UVW galactic velocities indicate this source probably belongs to the thin disk (Bensby et al. 2003). The catalog does not include star B, which hence acts as a contamination source to the reported information on this system. The Gaia data provides a large excess noise ($\epsilon_i = 3.1$) and a significance of the excess noise of $D > 10000$, which is an extremely large value. Also, the renormalized unit weight error (RUWE) parameter of ~ 30 is significantly larger than the threshold value of 1 expected for sources for which the single-star model provides a good fit to the astrometric observations (Lindgren et al. 2021). This is compatible with the presence of KOI-3886 B and may be influenced by the asteroseismic modulations in KOI-3886 A and the eclipse variations detected in the *Kepler* light curve. Additionally, the Gaia catalog indicates the presence of another two close-by sources (Gaia EDR3 2082127547280244224 and Gaia EDR3 208212747855928448) located ~ 1.7 arcmin from the KOI-3886 system. According to the EDR3 catalog, these sources are both at around 650 pc (one of which is possibly an M dwarf), with very similar proper motions as KOI-3886 ($\mu_{\alpha} = -10.2$ mas/yr, $\mu_{\delta} = -2.8$ mas/yr and $\mu_{\alpha} = -6.5$ mas/yr, $\mu_{\delta} = +3.4$ mas/yr). This distance, as shown in Sect. 5, is perfectly compatible with that estimated for our target system. The projected separation corresponds to 74 000 au, hence one-fourth of the Sun-Proxima Centauri distance. However, since these targets are not included in the *Kepler* aperture we do not consider them in the subsequent analysis. But we want to highlight that their presence could make this system even more interesting dynamically speaking.

3. An impostor planet

3.1. The planet-like signal

We used the preliminary RVs derived in Sect. 2.4 to perform a first stand-alone analysis of the data. The RVs show a clear modulation with the same periodicity as the transit signal seen in the *Kepler* and TESS data. We first modeled the dataset using a one-Keplerian model with a uniform prior on the orbital configuration (eccentricity and argument of the periastron) and RV semi-amplitude. The tidal modulation induced by the planet candidate into the stellar photosphere also creates an ellipsoidal shape in the star that affects the RV. We accounted for this effect by adding a second term to the RV signal as in Arras et al. (2012), which has a periodicity corresponding to twice the orbital period. We used a uniform prior between 0 and 100 m/s for the semi-amplitude of the tide. The parameter space was explored using a Markov Chain Monte Carlo (MCMC) scheme using the *emcee* implementation (Foreman-Mackey et al. 2013). We used four times the number of parameters as walkers ($N_w = 40$) and 20 000 steps per walker. After a first exploration of the parameter space, we performed a burn-in phase and then focused on

a small region around the maximum-likelihood solution to obtain reliable uncertainties to our parameters. The solution does not constrain the eccentricity of the orbit of the planet. Hence, we proceeded with a pure circular orbit for the planet. The solution provides a larger Bayesian evidence (estimated through the `perrakis` code, Perrakis et al. 2014) for the circular model. The results of this model show a Keplerian signal with a semi-amplitude RV of $K = 150.8 \pm 7.2$ m/s. The tidal effect induced a clear signal of $K_{\text{tide}} = 15.2 \pm 7.3$ m/s. Assuming the stellar properties published in the *Kepler* Input Catalog (Brown et al. 2011), the Keplerian signal corresponds to a minimum mass for the planet candidate of $m_p \sin i = 1.83 \pm 0.14 M_J$.

Separately, we also explored the *Kepler* light curve in a stand-alone fashion. The light curve from KOI-3886 contains several effects that deserve preliminary qualitative discussion. The out-of-eclipse light curve shows a double hump typical of ellipsoidal modulations. Both peaks are located at quadrature phases ($\phi = 0.25$ and $\phi = 0.75$), as expected for a circular or near-circular orbit. Also, their amplitudes are slightly different, hence we expect the Doppler beaming to play a role. The flux at mid-phase ($\phi = 0.5$) is compatible with the flux just before or after the transit, hence the reflection component seems negligible. Additionally, stellar pulsations are evident in the light curve and even clearer in the periodogram. Their amplitudes are relatively large compared to the ellipsoidal amplitude and transit depth. Hence, the detection of individual transits is blurred by these oscillations. The transit signal in the phase-folded light curve (where pulsation effects are averaged out) shows a clear asymmetric shape, with the egress longer than the ingress. This asymmetry can be interpreted as a non-zero orbital eccentricity (e.g., Kane & von Braun 2008). However, the difference in duration of both effects would imply an eccentricity that is too large and incompatible with the RV data and the dynamical analysis of the system, which should have circularized the orbit already (unless it is currently decaying fast to the host star). Alternatively, the asymmetry could come from an extended cometary-like tail as in the case of evaporating planets (e.g., Bourrier et al. 2015). A third possibility would be the tidal effect exerted by the star, which would make the planet shape to stretch in the planet-star direction. However, in a circular orbit, this would lead to symmetric ingress and egress shapes. A small but not null eccentricity might explain the asymmetry.

In order to average out the large photometric variations due to the stellar pulsations, we phase-folded the *Kepler* light curve with the eclipse period and binned the dataset in phase to reach 1 000 data points. This means an average binning of 67 data points per bin in phase. With this approach we effectively removed the large asteroseismic variations. We then proceeded with a simple analysis of the whole *Kepler* dataset including the reflexion, ellipsoidal, and beaming (hereafter REB) modulations and the transit and eclipse model. For the REB modulations, we used the equations and parametrization from Lillo-Box et al. (2014a) and for the transit and eclipse signals we used the `batman` code (Kreidberg 2015). We used `emcee` to model the data, and used a prior for the inclination that ensured a non-grazing transit. The posterior distribution of the parameters converged appropriately except for the inclination, which tends to get below the allowed range toward more inclined values implying a grazing eclipse. The results for the planet mass and radius from the light curve modeling show a strong degeneracy between different parameters, but pointed to a large $R_p > 2.5 R_{Jup}$ and massive ($> 1 M_{Jup}$) planet, in relative agreement with the RV analysis.

Based on these results, this planet would have been the closest planet to a red giant star and its semimajor axis placed it as the closest planet to the Roche Lobe with $a/a_{RL} = 1.2$, twice closer than the closest ones (Kepler-91 b at $a/a_{RL} = 2.3$; Lillo-Box et al. 2014a- and K2-141 b $a/a_{RL} = 2.2$; Malavolta et al. 2018). In terms of planet evolution, this would have been a major discovery, as we would be watching the planet death in real time. In this scenario (eclipsing object around KOI-3886 A), we can compute the dynamical evolution of the system as the star leaves the main sequence following Villaver & Livio (2009) and Villaver et al. (2014). We find that using a standard stellar evolution model and the measured parameters (an almost circular orbit with an initial period of 5.56 days) the planet would not have survived to the point at which the star reaches the current stellar radius of $11.2 R_{\odot}$. Instead, it would have been engulfed before, at approximately $R_{\star,A} = 8 R_{\odot}$, as a result of tidal forces. The planet would have fallen into the stellar envelope in only ~ 6 Myr. Such a short scale of evolution makes it very unlikely to observe phenomena like this. To force its survival to the current stellar radius-orbit ratio we have to use a larger initial orbit (0.1 au versus the 0.07 au) or force the standard tidal parameters to such values that basically inhibit tidal decay as the star evolves off the main sequence. All this made the planet scenario around KOI-3886 A very challenging and unlikely, pointing to alternative solutions.

3.2. The false positive detection

Despite the clear signs that the eclipsing object has a planetary nature in both the RV and photometric time series, the presence of a very close companion to the main target and its relatively small contrast made it necessary to analyze the data more in depth. The CCF for all spectra only shows one apparent sharp component, suggesting that only one of the two sources inside the fiber possesses a spectrum compatible with the lines in the binary mask, that is, a solar-like spectrum. However, we also estimated the bisector of the CCF to check for potentially blended components. By using the CCFs calculated with the G2 mask, we found a strong correlation of the bisector with the RVs, indicating that some deformation of the CCF profile was the responsible for the RV variations (see Fig. B.1). The correlation with the bisector is an indication of potential blending scenario similar to that observed in the HD 40114 system (Santos et al. 2002). Subsequently, we recomputed the CCF using different binary masks, namely from spectral types F9, G2, K2, and M0. We then computed the RVs from the entire wavelength range and also by splitting it into three different color chunks (blue: 3800-5100 Å, green: 5100-6400 Å, and red: 6400-7800 Å). In Fig. B.1 we show the results of this exercise. We can clearly see a dependence of the amplitude of the RV curve with the mask spectral type, increasing progressively toward bluer masks. Additionally, for a given mask, the bluer wavelength range produces larger amplitudes. All this is a clear indication of an additional hotter but shallower component in the CCF.

Consequently, we performed a two-component analysis of the CCF, including a sharp component and a broad shallower component (see an example in Fig. B.2). We fitted all CCFs obtained with the G-type mask from the HERMES instrument simultaneously with the full width at half maximum (FWHM) of the Gaussian profiles (σ_S - sharp - and σ_B - broad) as common parameters for all epochs, but letting the contrast, center, and level of the profiles free for each different epoch. With 20 epochs, we used an MCMC approach to obtain the posterior dis-

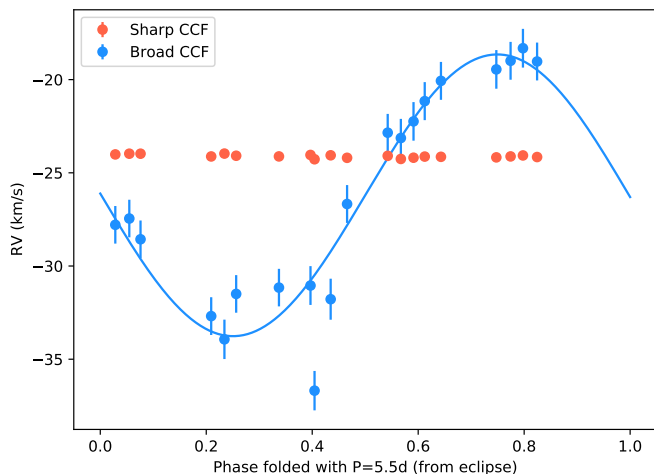


Fig. 7. Radial velocity variations of the two components of the CCF from the HERMES dataset phase-folded with the period from the eclipses seen in the *Kepler* time series.

tribution of all 123 parameters, including a jitter for the CCF for each epoch.

Interestingly, the MCMC was able to recover the second, very shallow component (ten times shallower than the sharper component and three times broader). The center of the Gaussian profile for each of the components determines the RV after the barycentric Earth RV correction is applied. Figure 7 shows both time series and the phase-folded RV curve assuming the period from the eclipse signal. From this figure, it becomes evident that the 5.6 day periodicity is actually occurring on the broad and shallow component, with a much larger RV semi-amplitude of ~ 7 km/s. This blended component combined with the sharp component was actually producing a planet-like signal that resulted in a semi-amplitude of 150 m/s, which is compatible with a planetary-like signal.

We thus conclude that the RV variations and the eclipses seen in the *Kepler* light curve are not due to a close-in planet but to an eclipsing binary whose CCF and light curve are diluted by a companion star. In the following sections we analyse the system taking this information into account to unveil which of the two stars (A or B) is the host of the eclipsing object and to characterize the properties of the system.

4. System parameters

4.1. Who is who?

From the above analysis we have several clues to solve the *who-is-who* in this system. We know that: i) there is an eclipsing system (Sect. 2.1), ii) there is only one giant star with $1.6 < \log g < 3.4$ since there is only one set of oscillation frequencies within the accessible range (see Fig. 4 and Sect. 2.1), iii) there is a hot component and a cold component from the SED (see Sect. 2.3 and 4.4.1), iv) the cold component is brighter and dominates the SED (Sect. 2.3 and 4.4.1), v) the hot component is the one hosting the eclipses (see Sect. 3.2), and vi) the star hosting the eclipses must be an evolved star ($R > 2.3 R_{\odot}$ for $M > 1 M_{\odot}$) to account for the amplitude of the ellipsoidal modulations displayed at the given periodicity.

With all this information we build a decision tree to unveil the relative location of stars A and B to clarify the system architecture. This is shown in Fig. 8 where we use the above ar-

guments to discard the different possible scenarios. In summary, the only branches that we cannot discard based on the data indicate that star A is the giant star producing the pulsations and that star B is the star hosting the eclipses and should hence also be an evolved star. From these data, however, it is not possible to discern whether components A and B are actually bound or if they are simply a chance alignment, in which case star B is slightly closer in the first branch, although it cannot be too far from star A because otherwise it would be a main-sequence star, which is incompatible with the ellipsoidal modulations at that periodicity; or star B could be farther away in the third branch. Equivalently, it cannot be too far away because otherwise it would be a super-giant star, which is incompatible with the ellipsoidal and RV data.

However, the unbound (chance-aligned) scenario in both cases seems unlikely because of stellar population statistics. In order to quantify this argument, we can estimate the probability of having two evolved stars at a separation below 1 arcsec in this region of the sky. We followed a similar procedure as that described in Lillo-Box et al. (2014b) and also used in other works (e.g., Themessl et al. 2018). Such probability is given by $P_{\text{chance}} = \pi r^2 \rho_{\text{evolved}}$, where r is the maximum radius to compute the probability and ρ_{evolved} is the density of evolved stars in the region. Since the separation between star A and B is 0.43 arcsec, we can conservatively use $r = 0.5$ arcsec. To estimate ρ_{evolved} we used the TRILEGAL² galactic model (v1.6, Girardi et al. 2012) to retrieve a simulated stellar population around the location of the KOI-3886 system. We used the *astrobase* implementation (Bhatti et al. 2020) to simulate such population and compute the density of stars around the target position. We simulated stars up to magnitude $V = 20$ mag and selected only those with $\log g < 4$ to conservatively include evolved stars from the subgiant phase. By using this, we obtain a density of 6200 evolved stars per deg^2 . By applying the above equation, we obtain a probability of chance alignment of two evolved stars within 0.5 arcsec to be 0.038%. This can be interpreted as a probability of 99.96% of the two evolved stars being actually bound.

Given these numbers, we conclude that the most plausible scenario for the KOI-3886 system is that both components KOI-3886 A and KOI-3886 B are bound (and hence are coeval), where KOI-3886 A is a giant star showing solar-like pulsations (Sect. 4.3) and KOI-3886 B is a subgiant star hosting KOI-3886 C. The bound scenario is also reinforced by the very similar systemic RV of both components around -25 km/s as shown in Fig. 7. Figure 9 shows a schematic view of the system given the above-mentioned architecture and including the information on the individual components derived in the subsequent sections.

4.2. Spectroscopic analysis

Among the two bright stars in the KOI-3886 system, the sharp component from the CCF analysis (corresponding to KOI-3886 A as demonstrated in 4.1) is the one that dominates the spectrum owing to its largest contrast and narrower spectral lines. Hence, in this section we consider only this source (star A) and neglect the possible effects in the spectrum due to the shallow component (star B).

We derived the stellar atmospheric parameters (T_{eff} , $\log g$, micro-turbulence, [Fe/H]) and respective uncertainties using the ARES and MOOG codes, following the same methodology described in Sousa (2014) and Santos et al. (2013). The equivalent widths (EW) of iron lines were measured on the combined

² <http://stev.oapd.inaf.it/cgi-bin/trilegal>

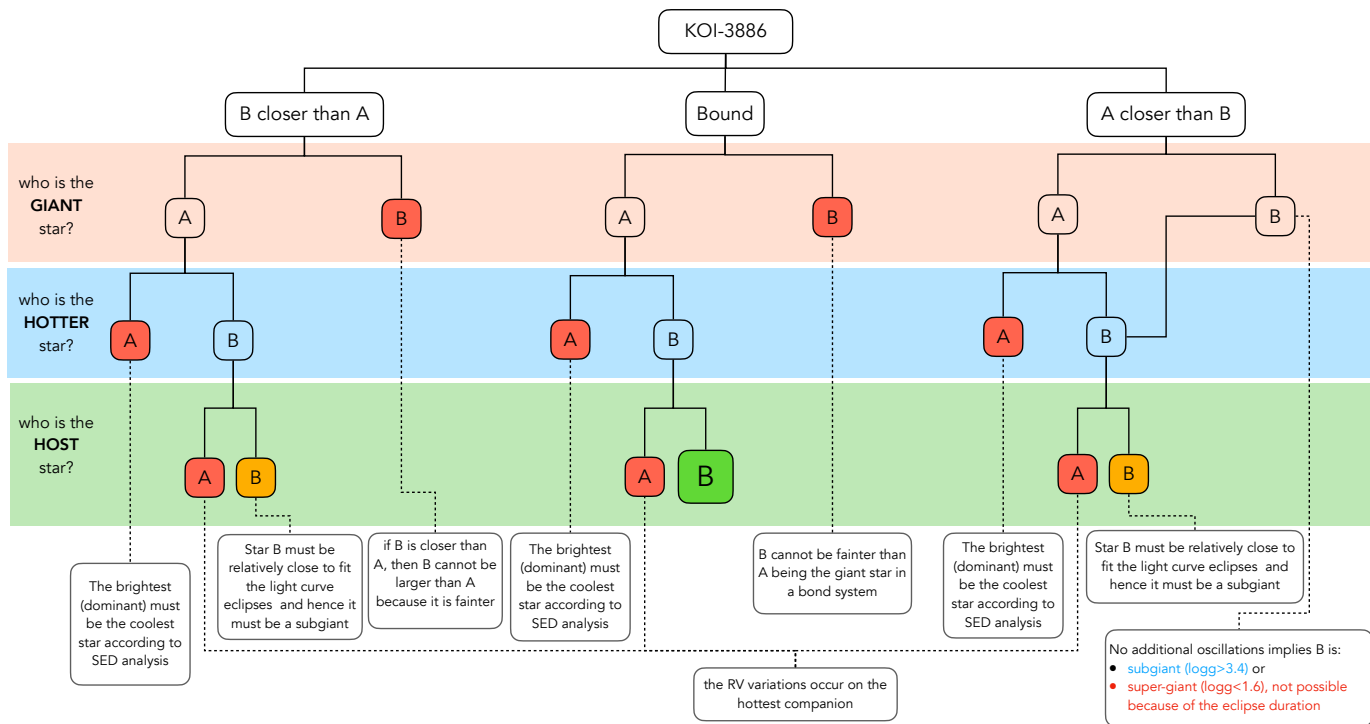


Fig. 8. Decision tree diagram to unveil the KOI-3886 system. The red boxes represent the invalid branches and the reasons are provided in the linked boxes using dashed lines. The green box is the preferred scenario owing to the probabilistic reasons provided in Sect. 4.1. The branches finishing in orange boxes cannot be discarded although they seem unlikely owing to these probabilistic arguments.

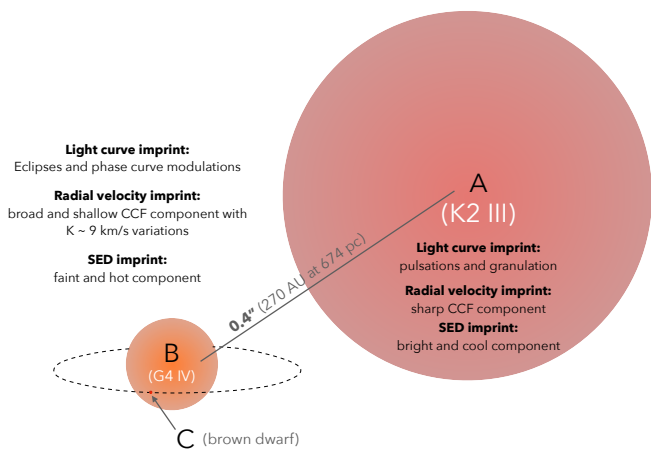


Fig. 9. Schematic view of the hierarchical triple scenario inferred for the KOI-3886 system; component A is a ~K2 III giant star accompanied by an eclipsing binary star composed by a ~G4 IV subgiant star eclipsed by a late-type M8-L3 dwarf star. The size of the three components is scaled to their actual sizes as determined in this paper.

CAFE spectrum of KOI3886 using the ARES code³ (Sousa et al. 2007, 2015). We used a minimization process to find ionization and excitation equilibrium and converged to the best set of spectroscopic parameters. This process makes use of a grid of Kurucz model atmospheres (Kurucz 1993) and the radiative transfer code MOOG (Snedden 1973). Since the star is cooler than 5200 K we used the appropriate iron line list for our method presented

³ The last version of ARES code (ARES v2) can be downloaded at <http://www.astro.up.pt/~sim@sousasag/ares>

Table 2. Spectroscopic (Sect. 4.2) and asteroseismology (Sect. 4.3) parameters of KOI-3886 A.

Parameter	KOI-3886 A
<i>Spectroscopy</i>	
Effective temperature, $T_{\text{eff},A}$	4720 ± 120 K
Surface gravity, $\log g_A^{\text{spec}}$	2.54 ± 0.24
Turbulent velocity, v_{turb}	1.172 ± 0.095 km/s
Metallicity, [Fe/H]	0.143 ± 0.065
<i>Asteroseismology</i>	
Stellar mass, $M_{\star,A}$	$1.69^{+0.14}_{-0.10} M_{\odot}$
Stellar radius, $R_{\star,A}$	$11.13^{+0.32}_{-0.26} R_{\odot}$
Stellar luminosity, $L_{\star,A}$	$55.1^{+5.2}_{-2.4} L_{\odot}$
Surface gravity, $\log g_{\star,A}^{\text{ast}}$	$2.577^{+0.011}_{-0.009}$
Stellar age	$2.05^{+0.56}_{-0.28}$ Gyr

in Tsantaki et al. (2013). The results of this analysis are shown in the upper part of Table 2 and point to the spectrum dominant star (KOI-3886 A) to be an early-K type star ascending the RGB, hence being the source of the solar-like oscillations seen in the *Kepler* light curve.

4.3. Asteroseismology

KOI-3886 A was previously classified as a first-ascent red giant by several authors (Elsworth et al. 2017; Hon et al. 2017; Vrad et al. 2018) based on the analysis of its oscillation spectrum. The star physical parameters were previously determined through scaling relations to be $M_{\star,A} = 1.81 \pm 0.11 M_{\odot}$ and

$R_{\star,A} = 11.61 \pm 0.25 R_{\odot}$ (Yu et al. 2018). In this work, we make use of this prior information regarding the evolutionary state of the star to conduct a detailed asteroseismic analysis and determine precise stellar fundamental properties (full details of the analysis will be presented in a follow-up paper; T. Campante et al. 2021, in preparation).

We based our analysis on a custom *Kepler* light curve generated by the KADACS pipeline (*Kepler* Asteroseismic Data Analysis and Calibration Software; García et al. 2011, 2014) spanning nearly four years. Figure 4 shows the corresponding power spectrum, which reveals a clear power excess due to solar-like oscillations at $\sim 50 \mu\text{Hz}$. We measured the large frequency separation, $\Delta\nu$, and the frequency of maximum oscillation amplitude, ν_{max} , using well-tested automated methods (Campante et al. 2017, 2019; Corsaro et al. 2020), which returned $\Delta\nu = 4.60 \pm 0.20 \mu\text{Hz}$ and $\nu_{\text{max}} = 46.9 \pm 0.3 \mu\text{Hz}$. We next extracted individual mode frequencies from the power spectrum using the FAMED pipeline (Fast and AutoMated pEak bagging with DIAMONDS; Corsaro et al. 2020). A total of 34 modes of angular degree $\ell = 0, 1$, and 2 (including a number of mixed $\ell = 1$ modes) were extracted across seven radial orders (see Fig. B.3).

A grid-based inference procedure was used to determine the fundamental properties of KOI-3886 A. It consisted in fitting the individual oscillation frequencies along with the classical constraints T_{eff} , $\log g$, and $[\text{Fe}/\text{H}]$, following the approach described in Li et al. (2020), without considering interpolation and setting the model systematic uncertainty to zero. The grid of stellar models was computed with recourse to the Modules for Experiments in Stellar Astrophysics (MESA, version 12115) (Paxton et al. 2011, 2013, 2015, 2018) and the corresponding adiabatic model frequencies with GYRE (version 5.1; Townsend & Teitler 2013). The microscopic and macroscopic physics adopted in the construction of the grid followed closely that described in Li et al. (2020), but a different solar chemical mixture was considered, namely, $[(Z/X)_{\odot} = 0.0181]$ provided by Asplund et al. (2009). Models in the grid varied in stellar mass (M_{\star}) within $0.8 - 2.2 M_{\odot}$ in steps of $0.02 M_{\odot}$, initial helium fraction (Y_{init}) within $0.24 - 0.32$ in steps of 0.02 , initial metallicity ($[\text{Fe}/\text{H}]$) within $-0.5 - 0.5$ in steps of 0.1 . Moreover, four values were considered for the mixing length parameter associated with the description of convection, namely, $\alpha_{\text{MLT}} = 1.7, 1.9, 2.1, \text{ and } 2.3$. We considered convective overshooting in the core and applied the exponential scheme given by Herwig (2000). We set up the overshooting parameter as a function of the mass $f_{\text{ov}} = (0.13M - 0.098)/9.0$ and used a fixed f_{ov} of 0.018 for models with a mass above $2.0 M_{\odot}$, following the mass-overshooting relation found by Magic et al. (2010).

The stellar properties inferred from our modeling procedure are shown at the bottom part of Table 2. These were obtained from the corresponding probability density distributions, where the value corresponds to the median and the uncertainties to the 16th and 84th percentiles, respectively. The frequencies of a representative best-fitting model are shown in the échelle diagram in Fig. B.3 for comparison with the observed frequencies.

We should note at this point that no other seismic signal is seen in the power spectrum. This null detection is consistent with the stellar parameters obtained for KOI-3886 B in Sect. 4. By using the relation $\nu_{\text{max}} \propto g * T_{\text{eff}}^{-1/2}$ scaled by solar values (Brown et al. 1991; Belkacem et al. 2011), this gives an expected ν_{max} for KOI-3886 B of $\sim 370 \mu\text{Hz}$. This is above the Nyquist frequency of *Kepler*'s 30-min cadence data of $280 \mu\text{Hz}$ (see Fig. 4). Even with a faster cadence (and hence higher Nyquist frequency), the

wash-out (dilution) from the primary would make oscillations in KOI-3886 B likely non-detectable.

4.4. Global stellar parameters

The procedure to compute the whole set of parameters for stars A and B, and object C requires feedback between (1) the combined spectroscopic and asteroseismology analysis (Sects. 4.2 and 4.3), (2) the SED fitting (Sect. 4.4.1), (3) the analysis of the light curve (Sect. 4.5), and (4) the spectral fitting (Sect. 4.4.2). Our analysis consisted of the following steps: i) The parameters of star A ($T_{\text{eff},A}$, $\log g_{\star,A}$) derived from (1) are used as constraints in (2) to estimate $T_{\text{eff},B}$; (2) is not very sensitive to stellar gravity and metallicity, therefore these parameters cannot be obtained in the first step. ii) The age of the system estimated from (1), and the value of $T_{\text{eff},B}$, put limits in the Hertzsprung-Russell (HR) diagram $\log g_{\star} - T_{\text{eff}}$ to the position of star B, which is used to set a constraint to the priors for the mass and radius of this star to be used in (3). iii) The analysis in (3) provides constraints on ($M_{\star,B}$, $R_{\star,B}$) and ($M_{\star,C}$, $R_{\star,C}$). The values for star B are used to refine the results from (2). iv) The position of star A in the HR diagram is refined by assuming that both A and B are coeval, and hence both should belong to the same isochrone. This allows us to recompute ($M_{\star,A}$, $R_{\star,A}$). v) Using the values of (T_{eff} , $\log g_{\star}$) for stars A and B, and the contrast at every wavelength from (2), a combined model spectrum for A and B are built and compared with the observed spectrum. This is a mandatory control to ensure the quality of the fit. vi) The results (T_{eff} , R_{\star}) for A and B can be used to compute the corresponding luminosities. Making use of the integration of the models obtained in (2), an estimate of the distance to both stars – a parameter that *never* enters the analysis – is feasible. Since the working hypothesis is that the system is bound, slight refinements of the parameters are carried out until the values of the distances are the same, within the uncertainties, and the whole set of parameters is self-consistent.

In the following subsections, we give some specific details of the procedures (2) SED fitting and (4) spectral fitting.

4.4.1. SED fitting

The photometry in Table A.1 corresponds to the combined light of stars A and B, plus the eclipsing object C. Therefore we attempted to carry out a two-model fit fulfilling some observational constraints⁴. Since data in the $i'K_s$ bands (corresponding to the combined light of stars A and B) are available (Table A.1), and the contrasts between the fluxes of both objects in these bands are known from Robo-AO (i' , 1.13 mag, Ziegler et al. 2017) and PHARO (K_s , 2.23 mag, Furlan et al. 2017⁵), the first constraint to build a composite model is that the individual models reproduce the fluxes at ($i'K_s$)(A) and ($i'K_s$)(B). A second constraint is that the contribution of the model of star B compensates the deficit of flux at wavelengths shorter than 5000 \AA and, in particular, the NUV point that star A cannot account for. The third constraint is that during the fitting procedure, the models for both stars are reddened with the same value of the color excess $E(B-V)$ since we work under the hypothesis that the system is bound (see Sect. 4.1); that is, both stars are at the same distance, so they must undergo the same interstellar

⁴ The contribution of object C to the total flux at any wavelength is negligible.

⁵ <https://vizier.u-strasbg.fr/viz-bin/VizieR-3?-source=J/AJ/153/71/table8>

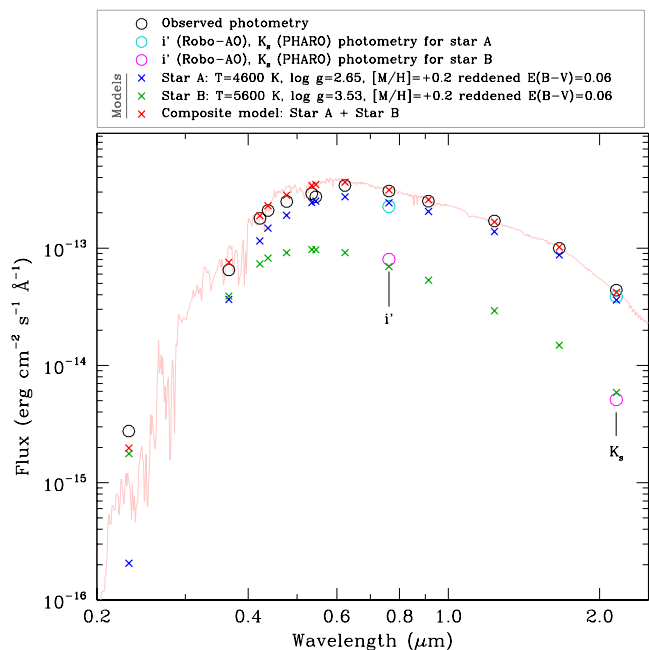


Fig. 10. Final result of the iterative process fitting the SED. The observed photometry is plotted as empty black circles, empty cyan and purple circles represent the fluxes at $i'K_s$ for stars A and B, respectively. The synthetic photometry on the models for stars A and B and the composite –final– model are plotted as blue, green, and red crosses. The composite model is also plotted in pale red.

absorption. Synthetic Castelli-Kurucz ATLAS9 models (Castelli & Kurucz 2003) are used throughout.

Table 3. Parameters of stars A and B as derived in Sect. 4.4.

Star	T_{eff} (K)	M_*/M_{\odot}	R_*/R_{\odot}	L_*/L_{\odot}
A	4600 ± 100	1.75 ± 0.10	10.40 ± 0.10	43.3 ± 9.5
B	5600 ± 100	1.61 ± 0.05	3.61 ± 0.09	11.5 ± 1.0

Table 3 and Fig. 10 show the final result of the iterative process fitting the SED. The observed photometry is plotted as empty black circles, empty cyan and purple circles represent the fluxes at $i'K_s$ for stars A and B, respectively, computed from the contrasts provided by the high-resolution imaging observations; the synthetic photometry on the models for stars A and B, both of which are reddened with $E(B-V) = +0.06$, are plotted as blue and green crosses, respectively, and the composite final model is plotted as red crosses and as a pale red line⁶. It is apparent that the final model, although approaching the observed GALEX NUV flux, does not quite reach that value; forcing the model to do so would push upward the fluxes at wavelengths around 4000 Å, worsening the overall quality of the fit. A possible reason for the deficit of NUV flux could be the fact that the models used are purely photospheric; that is, they do not take into account any effect in the UV continuum from the presence of a chromosphere. Franchini et al. (1998) carried out a comparison between observed and computed UV SEDs for a sample of 53 field G-

⁶ The GALEX NUV filter is so broad (FWHM ≈ 800 Å), and the SED so steep in this region that the point representing the synthetic photometry at this band, plotted at the effective wavelength of this filter does not lie on the low-resolution model itself

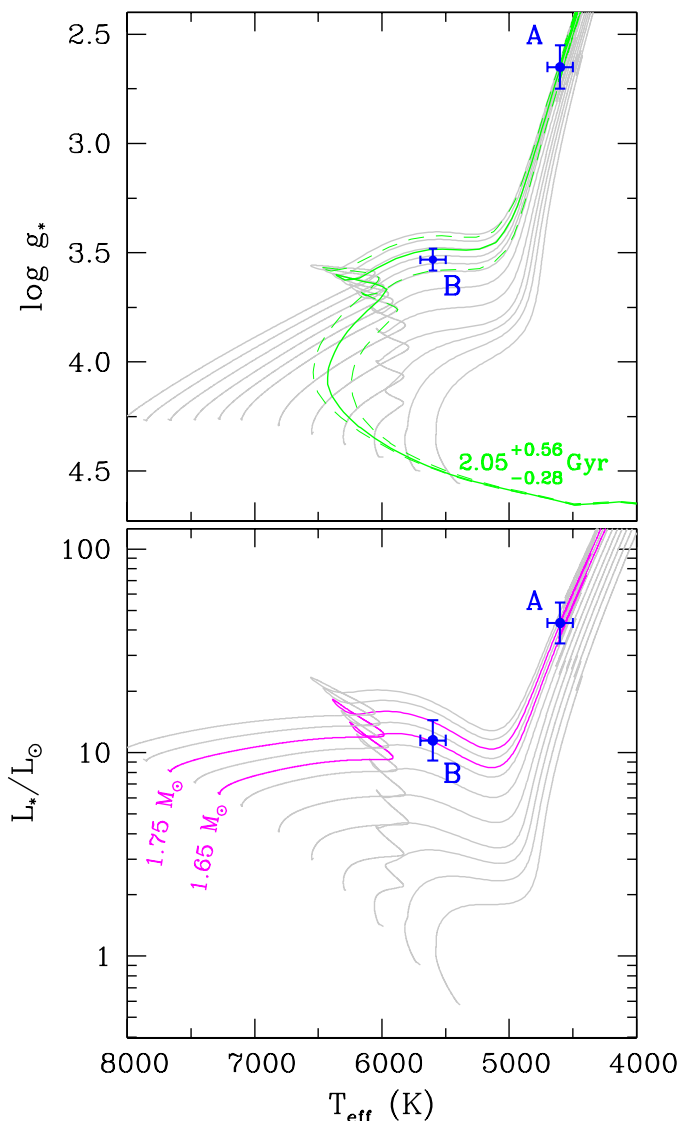


Fig. 11. Position of the stars in the HR diagram. PARSEC 2.1s tracks and isochrones with $Z = 0.03$ have been used. The location of the stars is consistent with the age found from the asteroseismology analysis (~ 2 Gyr). Tracks of masses 1.0, 1.1, 1.2, 1.3, 1.4, 1.5, 1.6, 1.65, 1.70, 1.75, 1.8, and 1.85 M_{\odot} are plotted.

type stars, concluding that UV excess shortward of 2000 Å was evident for all the program stars. Taking into account the star B is a G subgiant, the small remaining discrepancy between the observations and model could be explained in this context.

Figure 11 shows the position of stars A and B in the HR diagrams $\log g_* - T_{\text{eff}}$ and $L_*/L_{\odot} - T_{\text{eff}}$. PARSEC 2.1s tracks and isochrones⁷ (Bressan et al. 2012, 2013) have been used. During the iteration procedure it was found that a metallicity $Z = 0.03$ ($[M/H] \approx +0.2$) was more appropriate than the solar one, which agrees with the estimate from the asteroseismology analysis of star A (Sect. 4.3). In the top panel the isochrone $2.05^{+0.56}_{-0.28}$ Gyr from the asteroseismology analysis is plotted; the positions of the stars are totally consistent with that estimate.

A test about the robustness of the results is the computation of the distance to both stars, a parameter that did not enter and was not imposed at any moment in the calculations. From the

⁷ <https://people.sissa.it/~sbressan/parsec.html>

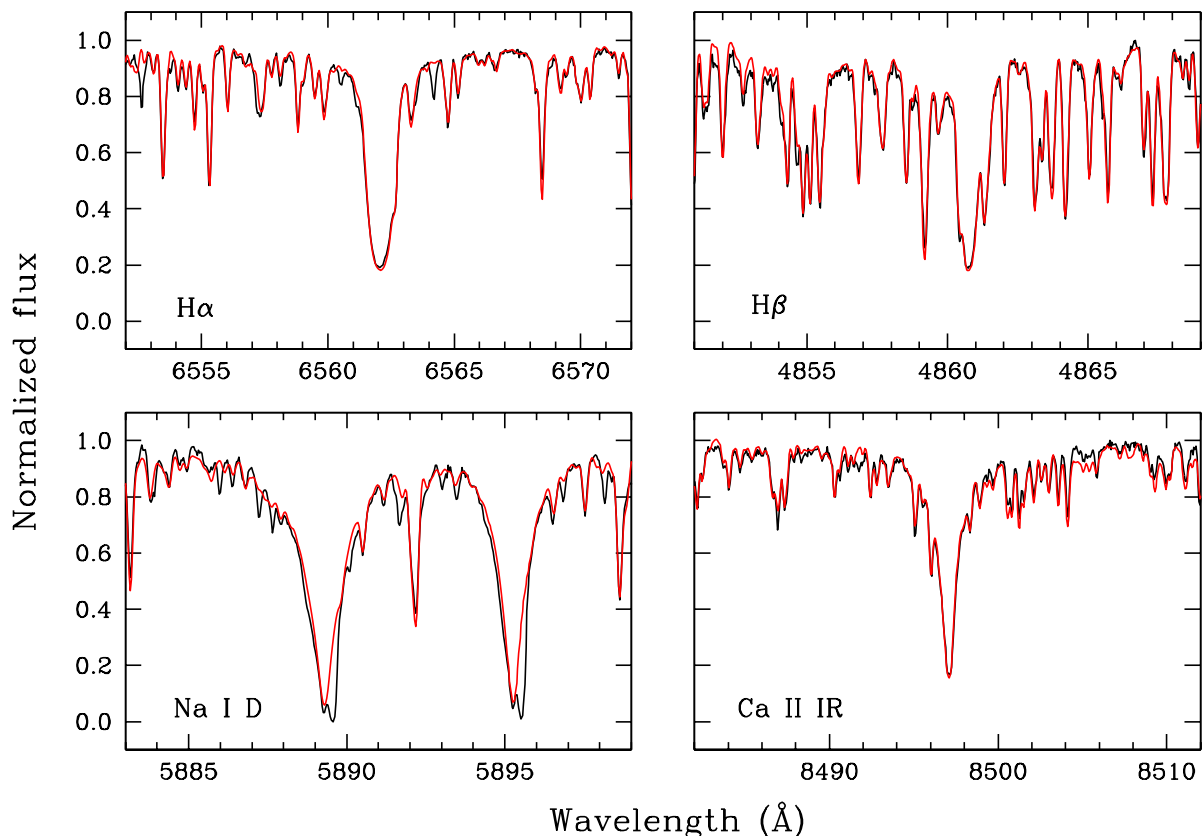


Fig. 12. CAFE spectrum of KOI-3886 (black) and the composite model built with the template spectra of real stars with types K2 III and G5 IV (red). Regions around H α , H β , Na I D, and the Ca II 8498 Å of the IR triplet lines are plotted.

values of T_{eff} and R_{\star} the stellar luminosity can be found using the well-known expression $L_{\star} = 4\pi\sigma R_{\star}^2 T_{\text{eff}}^4$. On the other hand the SED fitting provides us with models for the two stars, scaled to the observed photometry. Therefore the luminosity can also be written in terms of the integral of the dereddened model, F_{obs} , as $L_{\star} = 4\pi d^2 F_{\text{obs}}$; in both expressions of L_{\star} the only unknown is the distance, d . Using the corresponding numbers for each star we obtain $d_A = 685 \pm 75$ pc and $d_B = 662 \pm 29$ pc, that is, totally consistent with both stars being at the same distance. And interestingly, this is consistent within the uncertainties with the *Gaia* distance to the two other sources in the field described in Sect. 2.5, thus suggesting a potential even more complex multi-stellar system.

4.4.2. Spectral fitting

In this section we show the results of the comparison of the CAFE spectrum with a combination of spectra of real stars taken as templates. For this exercise, we used spectra of HD 140573 (K2 III) (star A) and HD 152311 (G5 IV) (star B). These spectra were downloaded from the ESO website⁸. The data in this collection were obtained with UVES/VLT, therefore the template spectra were mapped onto the resolution of the CAFE spectrograph.

Figure 12 shows the comparison of the CAFE spectrum and the composite spectrum from the templates. No relative shift in

RVs was applied when combining the spectra of the two stars. To carry out the combination, the template spectra of stars A and B were weighted at each wavelength according to the contrasts provided by the SED fitting.

The agreement between the CAFE spectrum and the composite model is remarkable, the only exception being the absorption at the red side of the two lines of the Na I doublet, at around +15 km/s, which is possibly caused by the interstellar medium.

4.5. Joint photometric and radial velocity analysis

Based on the information explained in the above sections, we performed a joint modeling of the *Kepler* light curve and both HERMES and CAFE RV data extracted using the two-component analysis of the CCF explained in Sect. 3.2. In order to avoid the large photometric variations due to the pulsations and granulation of the giant component KOI-3886 A, we used the phase-folded and binned *Kepler* light curve instead of the full dataset. In this case, we used the `ellc` package (Maxted 2016) to model the eclipse and phase curve variations. Given the effective temperature derived from the SED analysis for KOI-3886 B, we used a Gaussian prior for its mass centered at $1.6 M_{\odot}$ with a width of $0.1 M_{\odot}$ and truncated to ensure positive masses only. The priors on the radii of components B and C and the mass of component C were left uniform in a comprehensive range. We used Gaussian priors for the quadratic limb-darkening coefficients centered at the values estimated by the tables from Claret & Bloemen (2011) for the *Kepler* band in a trilinear interpolation with its effective temperature, surface gravity, and metallic-

⁸ Field Stars Across H-R Diagram:

http://www.eso.org/sci/observing/tools/uvespop/field_stars_uptonow.html

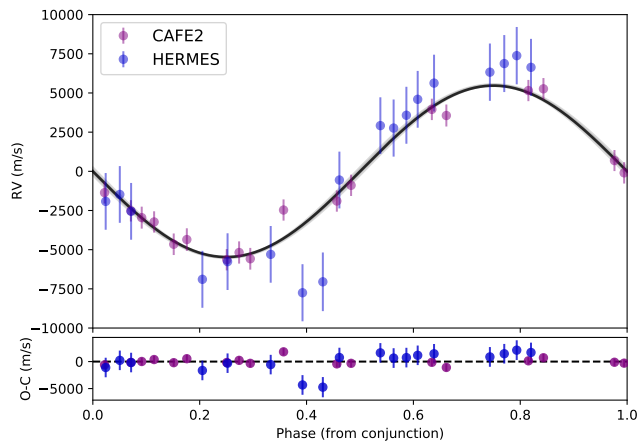


Fig. 13. Radial velocity of KOI-3886 B variations phase-folded with the orbital period of KOI-3886 C. The median model is shown as a solid black line and the corresponding 95% confidence interval is shown as a shaded gray region.

ity. The period and the mid-time of the primary eclipse were set to Gaussian distributions based on preliminary analysis of the light curve. Additionally, we included the flux ratio of components B to C as a free parameter with a flat prior on the whole possible physical range. Also, owing to the presence of KOI-3886 A inside the *Kepler* aperture, we added a dilution factor using the same definition as in Espinoza et al. (2019). Based on our multicolor, high spatial resolution images, we can provide an accurate prior for this factor by measuring the contrast magnitude between KOI-3886 A and KOI-3886 B in the *Kepler* band, which we estimate to be $\Delta m = 0.9$ mag. This implies a dilution factor of $\mathcal{D} = 0.28$. Finally, we added a flux level (F_0) and a jitter factor (σ_{Kepler}) for the photometric time series and a systemic velocity (δ) and jitter (σ) for each of the two RV instruments. The parameters and their priors are shown in Table A.2.

We used a MCMC approach to model this dataset by using the *emcee* package. In our final run, we used 70 walkers (four times the number of parameters) and a first burn-in phase with 40 000 steps followed by a final production step with 20 000 steps centered around the maximum probability parameter space found in the previous phase. This analysis leads to convergence of the chains. The marginalized posterior distribution of all parameters and their inter-dependences are shown in Fig. B.4 and the median and confidence intervals are presented in Table A.2. The results show that KOI-3886 C is an inflated brown dwarf ($M_{\star,C} = 66.1^{+4.1}_{-3.2} M_J$, $R_{\star,C} = 1.524 \pm 0.070 R_J$) orbiting close to the subgiant star KOI-3886 B. The median models for the light curve and RV signals are shown in Fig. 3 and Fig. 13, respectively.

5. Discussion

5.1. Eclipsing brown dwarf inflated by its subgiant host

Despite the initial planetary appearance of KOI-3886.01, the comprehensive analysis described in the previous sections shows a very different view of the overall system and, in particular, of the eclipsing object. The inferred mass of KOI-3886 C consistently estimated by the RV and phase-curve modulation effects provides a value of $66.1 \pm 3.5 M_J$. This value clearly places KOI-3886 C in the brown dwarf regime.

Eclipsing binaries, specifically those with an independent age estimate, are true Rosetta stones for improving evolutionary models and understanding the properties of isolated stars, such as the characteristics of their atmospheres, their evolution, and dependence on stellar mass. KOI-3886 is a unique system for the rare combination of its members and configuration: a giant $\sim K2$ III star, essential to accurately determine the system age plus an eclipsing pair, composed of a subgiant $\sim G4$ IV star and a brown dwarf, the spectral type of the latter probably being in the L-T transition (i.e., effective temperature below 2250 K); see Fig. 9.

Several studies have found eclipsing binaries in stellar associations whose ages are known. These are the cases of M11, a ~ 200 Myr old open cluster (see the case of KV29, a massive system Bavorsad et al. 2016); the Hyades, which is 625–790 Myr, and several interesting systems (HD 27130, which has a solar-like primary by Brogaard et al. 2021, and vA 50, a M4 plus, perhaps, a planet David et al. 2016); Praesepe, which is 600–800 Myr (several M-type binaries; Gillen et al. 2017); several young stellar associations such as UpperSco, 5–10 Myr (USco J161630.68–251220.1, a M5.5 primary with a very low-mass star close to the substellar limit, Lodieu et al. 2015; or the transiting brown dwarf RIK 72 b, David et al. 2019), or the first ever discovered eclipsing binary brown dwarfs, which is located in the 1 Myr massive association in Orion (Stassun et al. 2006b); and in globular clusters, such as NGC 6362, a 11.67 Gyr association that includes V40, a solar-like pair (Kaluzny et al. 2015).

In the field, other systems containing an eclipsing binary, which are interesting for different reasons, have been analyzed by Jackman et al. (2019b) or Lester et al. (2019b,a, 2020), just to provide a few examples. In particular, the combination of photometric, spectroscopic, and interferometric data (coming from the CHARA array, e.g.) can be used to provide a 3D orbit and greatly reduce the uncertainties of the system parameters. The advent of TESS has allowed detailed analysis of M plus brown dwarf pairs, such as those presented in Carmichael et al. (2019, 2020b, 2021). Of special interest is the triple system HIP 96515 (Huélamo et al. 2009), which contains an eclipsing binary composed by M1 and M2 dwarfs orbiting each other every 2.2456 days, and a white dwarf located at ~ 8 arcsec. In a sense, this system represents the future of KOI-3886 once the giant evolves and sheds its external layers.

In a mass-radius diagram (see Fig. 14, left panel), KOI-3886 C appears as the most inflated brown dwarf known to date. The incident flux received from its host star (KOI-3886 B) is about 2100 times that received by the Earth from the Sun, and is one of the most irradiated brown dwarfs known (see Fig. 14, right panel). This irradiation might well be the cause of the atmospheric inflation of this massive brown dwarf. KOI-3886 C is also the first brown dwarf known to eclipse an evolved star in the subgiant phase. The presence of the two evolved stars in the system, also makes KOI-3886 a dynamically and evolutionary interesting system to follow up.

5.2. Future evolution of the KOI-3886 system

We first consider the implications of the evolution of KOI-3886 B in the orbit of the substellar object, KOI-3886 C. In the current orbit, KOI-3886 C is unstable to tidal dissipation, so it will eventually experience orbital decay and end up inside the envelope of the subgiant. We estimated that the shrinking of the orbit from tidal decay takes 340 Myr from now, assuming a standard mass-loss rate for the star and typical tidal parameters. This is the time it takes to the star to evolve from the observed radius

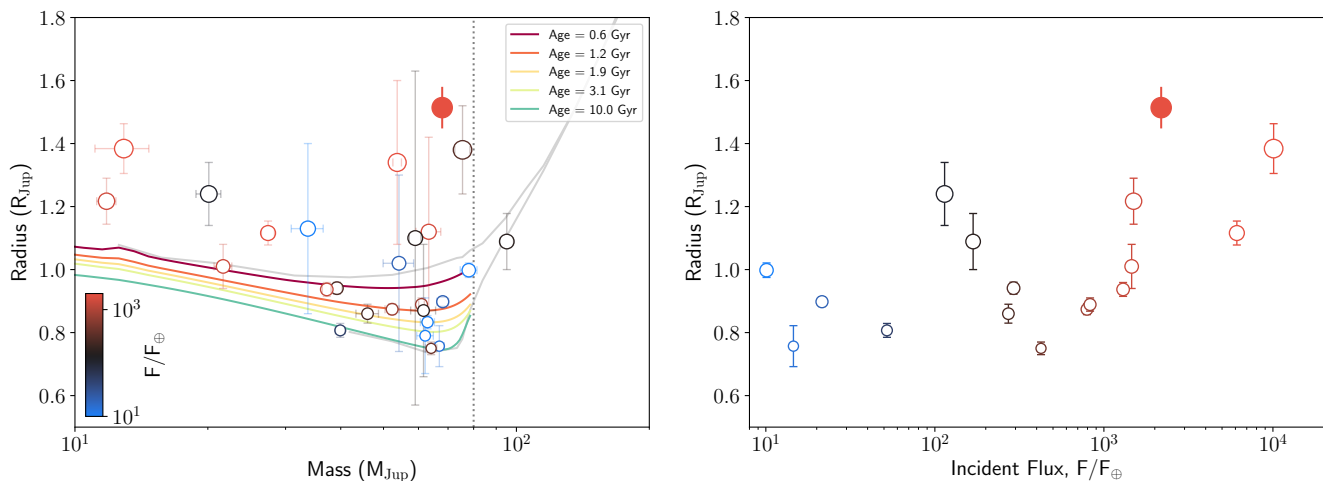


Fig. 14. Left panel: Mass-radius diagram in the brown dwarf regime for all known eclipsing brown dwarfs (open symbols) from Carmichael et al. (2020a) (and references there in) and the latest discoveries of TOI-503 (Šubjak et al. 2020), NGTS-7A (Jackman et al. 2019a), and TOI-263 (Parviainen et al. 2020; Palle et al. 2021). KOI-3886 C is represented by the filled symbol. The color code indicates the incident flux from their primary star in units of Earth’s flux received from the Sun. Isochrones for different ages from Phillips et al. (2020) are shown in colors, while the stellar tracks from Baraffe et al. (2015) for 1 and 12 Gyr are shown in gray. The dashed vertical line marks the hydrogen burning limit between stars and brown dwarfs. Right panel: Radius vs. incident flux of the same sample of brown dwarfs as in the left panel, showing the increasing evidence of irradiation as the source of inflation for these objects.

of $3.6 R_{\odot}$ to a stellar radius with a value of $8.9 R_{\odot}$. In its current state, we estimate the shrinking rate to be 7.4×10^{-9} au/yr, which translates into a period shrinking of 0.033 seconds/yr, which is difficult to measure in a decade time span.

Another issue altogether is the stability of C given that both B and C are in a binary system with the A component. The C component is in what is traditionally defined as a satellite-type or S-type orbit (Dvorak 1986), where the less massive body is orbiting the secondary star and the primary star can be considered as a perturber. From the empirical expressions of Holman & Wiegert (1999), we estimate the stable region around the subgiant for a circular binary orbit. We find the critical semimajor axis to be $a_C^{\text{crit}} = 27.35$ au, which is inside the orbital distance determined for the substellar object around the star B ($a_C = 0.159$ au).

The evolution of the binary is expected to modify the size of this stable region, and stellar evolution can trigger dynamical instabilities that drive planets into chaotic orbits. As the stars lose mass via winds, the mass ratio of the binary changes and with it the critical distance for stability (Kratter & Perets 2012). However, such a process does not happen in this system before C undergoes the orbital evolution described before. Although substantial mass-loss is responsible for a significant change in the critical stability radius, it does not occur until the star ascends the asymptotic giant branch after the red and horizontal branches. At that time, the substellar object is not expected to be orbiting the secondary, since as calculated before, it is engulfed well before the star B reaches the tip of the RGB.

6. Conclusions

In this paper we have unveiled the nature of the KOI-3886 system and planet candidate. Thanks to a large number of follow-up observations and analysis (mainly driven by the chromatic RV analysis and the use of different spectral masks to extract the RV; see Sect. 3.2), we could conclude that KOI-3886.01 is actually an eclipsing close-in brown dwarf (KOI-3886 C) orbiting a \sim G4 star in the subgiant phase (KOI-3886 B); both of these are bound to a \sim K2 star ascending the RGB (KOI-3886 A). The

eclipsing binary system has a projected separation to the RGB star of around 270 au. This relatively large separation implies an independent evolution of the binary system, not affected by the evolution and mass loss of the RGB star.

We inferred the properties of KOI-3886 A through a combination of spectroscopic, asteroseismic, and SED analysis, and conclude that this star has a radius of $10.4 R_{\odot}$, and an effective temperature of 4600 K and well-defined age of 2.05 Gyr. This star is the brightest of the two components seen in the high-spatial resolution images and is the dominant source in the optical spectrum of HERMES and CAFE data, corresponding to the sharp and narrow component of the CCF. Star KOI-3886 B on its side corresponds to the slightly fainter source in the high-resolution images and contributes to the spectrum with broader and shallower spectral lines. This is reflected in the CCF where this component shows large periodic RV variations coincident with the *Kepler* light curve eclipses. Through a thorough SED analysis, we could conclude that KOI-3886 B should be bounded to KOI-3886 A and, consequently, it must be in the subgiant phase with the same age. We infer an effective temperature of 5600 K for KOI-3886 B, making the secondary a \sim G4 IV star. The bound nature of the two evolved stars puts important constraints on the mass of KOI-3886 B, which become critical in estimating the mass of the eclipsing body. We used the RVs inferred from the HERMES and CAFE data and the *Kepler* light curve to perform a joint analysis, in which we were able to conclude that KOI-3886 B has a mass of $1.6 M_{\odot}$ and a radius of $3.61 R_{\odot}$, which agrees with its evolutionary stage. More importantly, we derive a mass of $66.1 M_J$ and a radius of $1.52 R_J$ to the third component in this system (KOI-3886 C), placing it in the brown dwarf regime. The inferred radius is about 50% larger than what theoretical models predict for this age. This inflation might be due to the strong stellar irradiation from KOI-3886 B given the close-in orbit of this system, which has an orbital period of just 5.6 days around a subgiant star.

The dynamical analysis of this system indicates that the eclipsing binary is stable for the next 340 Myr. After that, the evolution of KOI-3886 B will rapidly end in the disruption of

KOI-3886 C well before the B component reaches the tip of the RGB. The evolution of KOI-3886 A will not affect the dynamical stability of the binary at any stage before it reaches the tip of the AGB, which will happen way after the brown dwarf has been engulfed by its host.

KOI-3886 fully complements the parameter spaces left unpopulated by other systems and can be considered as a stepping stone, which will help improve the models. KOI-3886 C is the largest brown dwarf known to date and the first one known to eclipse an evolved star.

Acknowledgements. The authors thank the anonymous referee for taking the time to review this manuscript and the language editor for a thorough spelling and grammatical review. J.L.-B. acknowledges financial support received from "la Caixa" Foundation (ID 100010434) and from the European Union's Horizon 2020 research and innovation programme under the Marie Skłodowska-Curie grant agreement No 847648, with fellowship code LCF/BQ/PI20/11760023. This research has also been partly funded by the Spanish State Research Agency (AEI) Projects No.ESP2017-87676-C5-1-R and No. MDM-2017-0737 Unidad de Excelencia "María de Maeztu"- Centro de Astrobiología (INTA-CSIC). The work by B.M. and E.V. is partially funded by the Spanish "Ministerio de Ciencia, Innovación y Universidades" through the national project "On the Rocks II" (PGC2018-101950-B-I00; PI E. Villaver). This work was partially supported by FCT/MCTES through the research grants UIDB/04434/2020, UIDP/04434/2020 and PTDC/FIS-AST/30389/2017, and by FEDER - Fundo Europeu de Desenvolvimento Regional through COMPETE2020 - Programa Operacional Competitividade e Internacionalização (grant: POCI-01-0145-FEDER-030389). M.S.C. is supported by national funds through FCT in the form of a work contract. This work was supported by FCT - Fundação para a Ciência e a Tecnologia through national funds and by FEDER through COMPETE2020 - Programa Operacional Competitividade e Internacionalização by these grants: UID/FIS/04434/2019; UIDB/04434/2020; UIDP/04434/2020; PTDC/FIS-AST/32113/2017 & POCI-01-0145-FEDER-032113; PTDC/FIS-AST/28953/2017 & POCI-01-0145-FEDER-028953; PTDC/FIS-AST/28987/2017 & POCI-01-0145-FEDER-028987. T.C. is supported by Fundação para a Ciência e a Tecnologia (FCT) in the form of a work contract (CEECIND/00476/2018). A.A. acknowledges support from Government of Comunidad Autónoma de Madrid (Spain) through postdoctoral grant 'Atracción de Talento Investigador' 2018-T2/TIC-11697 T.L. acknowledges the funding from the European Research Council (ERC) under the European Union, Horizon 2020 research and innovation programme (Cartography GA. 804752). The research leading to these results has (partially) received funding from the European Research Council (ERC) under the European Union's Horizon 2020 research and innovation programme (grant agreement N°670519: MAMSIE) and from the KU Leuven Research Council (grant C16/18/005: PARADISE). Based on observations obtained with the HERMES spectrograph, which is supported by the Research Foundation - Flanders (FWO), Belgium, the Research Council of KU Leuven, Belgium, the Fonds National de la Recherche Scientifique (F.R.S.-FNRS), Belgium, the Royal Observatory of Belgium, the Observatoire de Genève, Switzerland and the Thüringer Landessternwarte Tautenburg, Germany. This work has made use of data from the European Space Agency (ESA) mission *Gaia* (<https://www.cosmos.esa.int/gaia>), processed by the *Gaia* Data Processing and Analysis Consortium (DPAC, <https://www.cosmos.esa.int/web/gaia/dpac/consortium>). Funding for the DPAC has been provided by national institutions, in particular the institutions participating in the *Gaia* Multilateral Agreement. We thank M. Günther for his help in using the *allesfitter* code (Günther & Daylan 2021, 2019), although we finally did not use it for other reasons. This work has made use of the following python packages: *astropy* (Astropy Collaboration et al. 2013, 2018), *numpy* (Harris et al. 2020), *batman* (Kreidberg 2015), *emcee* (Foreman-Mackey et al. 2013), *elc* (Maxted 2016), *matplotlib* (Hunter 2007), *astroML* (Vanderplas et al. 2012), and *corner* (Foreman-Mackey 2016).

References

Aceituno, J., Sánchez, S. F., Grupp, F., et al. 2013, *A&A*, 552, A31
 Aller, A., Lillo-Box, J., Jones, D., Miranda, L. F., & Barceló Forteza, S. 2020, *A&A*, 635, A128
 Arras, P., Burkart, J., Quartaert, E., & Weinberg, N. N. 2012, *MNRAS*, 422, 1761
 Asplund, M., Grevesse, N., Sauval, A. J., & Scott, P. 2009, *ARA&A*, 47, 481
 Astropy Collaboration, Price-Whelan, A. M., Sipőcz, B. M., et al. 2018, *AJ*, 156, 123
 Astropy Collaboration, Robitaille, T. P., Tollerud, E. J., et al. 2013, *A&A*, 558, A33

Baraffe, I., Homeier, D., Allard, F., & Chabrier, G. 2015, *A&A*, 577, A42
 Barclay, T., Rowe, J. F., Lissauer, J. J., et al. 2013, *Nature*, 494, 452
 Batalha, N. M., Rowe, J. F., Bryson, S. T., et al. 2013, *ApJS*, 204, 24
 Bavarsad, E. A., Sandquist, E. L., Shetrone, M. D., & Orosz, J. A. 2016, *ApJ*, 831, 48
 Beitia-Antero, L. & Gómez de Castro, A. I. 2016, *A&A*, 596, A49
 Belkacem, K., Goupil, M. J., Dupret, M. A., et al. 2011, *A&A*, 530, A142
 Bensby, T., Feltzing, S., & Lundström, I. 2003, *A&A*, 410, 527
 Bessell, M. S., Castelli, F., & Plez, B. 1998, *A&A*, 333, 231
 Bhatti, W., Bouma, L., Joshua, John, & Price-Whelan, A. 2020, *waqasbhatti/astrobase: astrobase v0.5.0*
 Borucki, W. J., Koch, D., Basri, G., et al. 2010, *Science*, 327, 977
 Bourrier, V., Lecavelier des Etangs, A., & Vidal-Madjar, A. 2015, *A&A*, 573, A11
 Bressan, A., Marigo, P., Girardi, L., Nanni, A., & Rubele, S. 2013, in *European Physical Journal Web of Conferences*, Vol. 43, *European Physical Journal Web of Conferences*, 03001
 Bressan, A., Marigo, P., Girardi, L., et al. 2012, *MNRAS*, 427, 127
 Brogaard, K., Pakštienė, E., Grundahl, F., et al. 2021, *A&A*, 645, A25
 Brown, T. M., Gilliland, R. L., Noyes, R. W., & Ramsey, L. W. 1991, *ApJ*, 368, 599
 Brown, T. M., Latham, D. W., Everett, M. E., & Esquerdo, G. A. 2011, *AJ*, 142, 112
 Campante, T. L., Corsaro, E., Lund, M. N., et al. 2019, *ApJ*, 885, 31
 Campante, T. L., Veras, D., North, T. S. H., et al. 2017, *MNRAS*, 469, 1360
 Carmichael, T. W., Latham, D. W., & Vanderburg, A. M. 2019, *AJ*, 158, 38
 Carmichael, T. W., Quinn, S. N., Mustill, A. J., et al. 2020a, *AJ*, 160, 53
 Carmichael, T. W., Quinn, S. N., Mustill, A. J., et al. 2020b, *AJ*, 160, 53
 Carmichael, T. W., Quinn, S. N., Zhou, G., et al. 2021, *AJ*, 161, 97
 Castelli, F. & Kurucz, R. L. 2003, in *Modelling of Stellar Atmospheres*, ed. N. Piskunov, W. W. Weiss, & D. F. Gray, Vol. 210, A20
 Claret, A. & Bloemen, S. 2011, *A&A*, 529, A75
 Cohen, M., Wheaton, W. A., & Megeath, S. T. 2003, *AJ*, 126, 1090
 Corsaro, E. & De Ridder, J. 2014, *A&A*, 571, A71
 Corsaro, E., McKeever, J. M., & Kuzlewicz, J. S. 2020, *A&A*, 640, A130
 David, T. J., Conroy, K. E., Hillenbrand, L. A., et al. 2016, *AJ*, 151, 112
 David, T. J., Hillenbrand, L. A., Gillen, E., et al. 2019, *ApJ*, 872, 161
 Dvorak, R. 1986, *A&A*, 167, 379
 Elsworth, Y., Hekker, S., Basu, S., & Davies, G. R. 2017, *MNRAS*, 466, 3344
 Espinoza, N., Kossakowski, D., & Brahm, R. 2019, *MNRAS*, 490, 2262
 Foreman-Mackey, D. 2016, *The Journal of Open Source Software*, 1, 24
 Foreman-Mackey, D., Hogg, D. W., Lang, D., & Goodman, J. 2013, *PASP*, 125, 306
 Franchini, M., Morossi, C., & Malagnini, M. L. 1998, *ApJ*, 508, 370
 Fukugita, M., Ichikawa, T., Gunn, J. E., et al. 1996, *AJ*, 111, 1748
 Furlan, E., Ciardi, D. R., Everett, M. E., et al. 2017, *AJ*, 153, 71
 García, R. A., Hekker, S., Stello, D., et al. 2011, *MNRAS*, 414, L6
 García, R. A., Mathur, S., Pires, S., et al. 2014, *A&A*, 568, A10
 Gillen, E., Hillenbrand, L. A., David, T. J., et al. 2017, *ApJ*, 849, 11
 Girardi, L., Barbieri, M., Groenewegen, M. A. T., et al. 2012, *Astrophysics and Space Science Proceedings*, 26, 165
 Günther, M. N. & Daylan, T. 2019, *Allesfitter: Flexible Star and Exoplanet Inference From Photometry and Radial Velocity*, *Astrophysics Source Code Library*
 Günther, M. N. & Daylan, T. 2021, *ApJS*, 254, 13
 Harris, C. R., Millman, K. J., van der Walt, S. J., et al. 2020, *Nature*, 585, 357
 Hernández Santisteban, J. V., Knigge, C., Littlefair, S. P., et al. 2016, *Nature*, 533, 366
 Herwig, F. 2000, *A&A*, 360, 952
 Holman, M. J. & Wiegert, P. A. 1999, *AJ*, 117, 621
 Hon, M., Stello, D., & Yu, J. 2017, *MNRAS*, 469, 4578
 Hornuth, F., Brandner, W., Hippler, S., & Henning, T. 2008, *Journal of Physics Conference Series*, 131, 012051
 Howell, S. B., Everett, M. E., Sherry, W., Horch, E., & Ciardi, D. R. 2011, *AJ*, 142, 19
 Huélamo, N., Vaz, L. P. R., Torres, C. A. O., et al. 2009, *A&A*, 503, 873
 Hunter, J. D. 2007, *Computing in Science & Engineering*, 9, 90
 Jackman, J. A. G., Wheatley, P. J., Bayliss, D., et al. 2019a, *MNRAS*, 489, 5146
 Jackman, J. A. G., Wheatley, P. J., Bayliss, D., et al. 2019b, *MNRAS*, 489, 5146
 Kaluzny, J., Thompson, I. B., Dotter, A., et al. 2015, *AJ*, 150, 155
 Kane, S. R. & von Braun, K. 2008, *ApJ*, 689, 492
 Kratter, K. M. & Perets, H. B. 2012, *ApJ*, 753, 91
 Kreidberg, L. 2015, *PASP*, 127, 1161
 Kurucz, R. L. 1979, *ApJS*, 40, 1
 Kurucz, R. L. 1993, *SYNTHES spectrum synthesis programs and line data*
 Law, N. M., Morton, T., Baranec, C., et al. 2014, *ApJ*, 791, 35
 Lester, K. V., Fekel, F. C., Mutterspaugh, M., et al. 2020, *AJ*, 160, 58
 Lester, K. V., Gies, D. R., Schaefer, G. H., et al. 2019a, *AJ*, 158, 218
 Lester, K. V., Gies, D. R., Schaefer, G. H., et al. 2019b, *AJ*, 157, 140
 Li, T., Bedding, T. R., Christensen-Dalsgaard, J., et al. 2020, *MNRAS*, 495, 3431

- Lillo-Box, J., Aceituno, J., Pedraz, S., et al. 2020, MNRAS, 491, 4496
- Lillo-Box, J., Barrado, D., Moya, A., et al. 2014a, A&A, 562, A109
- Lillo-Box, J., Barrado, D., & Bouy, H. 2012, A&A, 546, A10
- Lillo-Box, J., Barrado, D., & Bouy, H. 2014b, A&A, 566, A103
- Lillo-Box, J., Barrado, D., & Correia, A. C. M. 2016, A&A, 589, A124
- Lillo-Box, J., Millholland, S., & Laughlin, G. 2021, A&A, submitted
- Lindegren, L., Klioner, S. A., Hernández, J., et al. 2021, A&A, 649, A2
- Lodieu, N., Alonso, R., González Hernández, J. I., et al. 2015, A&A, 584, A128
- Magic, Z., Serenelli, A., Weiss, A., & Chaboyer, B. 2010, ApJ, 718, 1378
- Malavolta, L., Mayo, A. W., Loudon, T., et al. 2018, AJ, 155, 107
- Mann, A. W. & von Braun, K. 2015, PASP, 127, 102
- Maxted, P. F. L. 2016, A&A, 591, A111
- Mazeh, T., Nachmani, G., Sokol, G., Faigler, S., & Zucker, S. 2012, A&A, 541, A56
- Millholland, S. & Laughlin, G. 2017, AJ, 154, 83
- Olmedo, M., Lloyd, J., Mamajek, E. E., et al. 2015, ApJ, 813, 100
- Palle, E., Luque, R., Zapatero Osorio, M. R., et al. 2021, arXiv e-prints, arXiv:2103.11150
- Parviainen, H., Palle, E., Zapatero-Osorio, M. R., et al. 2020, A&A, 633, A28
- Paxton, B., Bildsten, L., Dotter, A., et al. 2011, ApJS, 192, 3
- Paxton, B., Cantiello, M., Arras, P., et al. 2013, ApJS, 208, 4
- Paxton, B., Marchant, P., Schwab, J., et al. 2015, ApJS, 220, 15
- Paxton, B., Schwab, J., Bauer, E. B., et al. 2018, ApJS, 234, 34
- Perrakis, K., Ntzooufras, I., & Tsonas, E. G. 2014, Computational Statistics & Data Analysis, 77, 54
- Phillips, M. W., Tremblin, P., Baraffe, I., et al. 2020, A&A, 637, A38
- Raskin, G., van Winckel, H., Hensberge, H., et al. 2011, A&A, 526, A69
- Ricker, G. R., Winn, J. N., Vanderspek, R., et al. 2014, in Society of Photo-Optical Instrumentation Engineers (SPIE) Conference Series, Vol. 9143, Society of Photo-Optical Instrumentation Engineers (SPIE) Conference Series, 20
- Santos, N. C., Mayor, M., Naef, D., et al. 2002, A&A, 392, 215
- Santos, N. C., Sousa, S. G., Mortier, A., et al. 2013, A&A, 556, A150
- Snedden, C. A. 1973, PhD thesis, THE UNIVERSITY OF TEXAS AT AUSTIN.
- Sousa, S. G. 2014, ARES + MOOG: A Practical Overview of an Equivalent Width (EW) Method to Derive Stellar Parameters, 297–310
- Sousa, S. G., Santos, N. C., Adibekyan, V., Delgado-Mena, E., & Israelian, G. 2015, A&A, 577, A67
- Sousa, S. G., Santos, N. C., Israelian, G., Mayor, M., & Monteiro, M. J. P. F. G. 2007, A&A, 469, 783
- Stassun, K. G., Mathieu, R. D., & Valenti, J. A. 2006a, Nature, 440, 311
- Stassun, K. G., Mathieu, R. D., & Valenti, J. A. 2006b, Nature, 440, 311
- Themssl, N., Hekker, S., Mints, A., et al. 2018, ApJ, 868, 103
- Townsend, R. H. D. & Teitler, S. A. 2013, MNRAS, 435, 3406
- Tsantaki, M., Sousa, S. G., Adibekyan, V. Z., et al. 2013, A&A, 555, A150
- Vanderplas, J., Connolly, A., Ivezić, Ž., & Gray, A. 2012, in Conference on Intelligent Data Understanding (CIDU), 47–54
- Villaver, E. & Livio, M. 2009, ApJ, 705, L81
- Villaver, E., Livio, M., Mustill, A. J., & Siess, L. 2014, ApJ, 794, 3
- Vrard, M., Kallinger, T., Mosser, B., et al. 2018, A&A, 616, A94
- Šubjak, J., Sharma, R., Carmichael, T. W., et al. 2020, AJ, 159, 151
- York, D. G., Adelman, J., Anderson, John E., J., et al. 2000, AJ, 120, 1579
- Yu, J., Huber, D., Bedding, T. R., et al. 2018, ApJS, 236, 42
- Ziegler, C., Law, N. M., Morton, T., et al. 2017, AJ, 153, 66

Appendix A: Tables

Appendix B: Figures

Table A.1. Photometry of KOI-3886.

λ (Å)	Magnitude	Flux (erg cm ⁻² s ⁻¹ Å ⁻¹)	Band	Source
2315.7	17.169±0.013	2.754(-15)±3.297(-17)	GALEX NUV [†]	Beitia-Antero & Gómez de Castro (2016)
3660	12.016±0.022	6.520(-14)±1.321(-15)	Johnson <i>U</i>	Bessell et al. (1998)
4220	11.447±0.091	1.794(-13)±1.505(-14)	Tycho <i>B</i>	Mann & von Braun (2015)
4380	11.198±0.027	2.097(-13)±5.214(-15)	Johnson <i>B</i>	Bessell et al. (1998)
4770	10.706±0.020	2.497(-13)±4.599(-15)	Sloan <i>g'</i>	Fukugita et al. (1996); York et al. (2000)
5350	10.352±0.054	2.914(-13)±1.450(-14)	Tycho <i>V</i>	Mann & von Braun (2015)
5450	10.306±0.050	2.739(-13)±1.262(-14)	Johnson <i>V</i>	Bessell et al. (1998)
6230	9.782±0.020	3.428(-13)±6.315(-15)	Sloan <i>r'</i>	Fukugita et al. (1996); York et al. (2000)
7620	9.465±0.020	3.069(-13)±5.653(-15)	Sloan <i>i'</i>	Fukugita et al. (1996); York et al. (2000)
9130	9.288±0.020	2.516(-13)±4.636(-15)	Sloan <i>z'</i>	Fukugita et al. (1996); York et al. (2000)
12350	8.159±0.020	1.705(-13)±3.141(-15)	2MASS <i>J</i>	Cohen et al. (2003)
16620	7.638±0.020	9.978(-14)±1.838(-15)	2MASS <i>H</i>	Cohen et al. (2003)
21590	7.475±0.023	4.383(-14)±9.284(-16)	2MASS <i>K_s</i>	Cohen et al. (2003)

[†] GALEX NUV magnitude is available from the Vizier catalog:

<https://vizier.u-strasbg.fr/viz-bin/VizieR?-source=J/ApJ/813/100>

Table A.2. Derived stellar parameters from components B and C of the KOI-3886 hierarchical triple system through the joint (RV, eclipse, and phase modulations) analysis presented in Sect. 4.5.

Parameter	Priors	Posteriors
<i>Orbital parameters</i>		
Orbital period, P_C [days]	$\mathcal{G}(5.56648691, 0.0001)$	$5.566513^{+0.000043}_{-0.000043}$
Time of mid-transit, $T_{0,C} - 2400000$ [days]	$\mathcal{G}(54966.03305, 0.008)$	$54966.0334^{+0.0012}_{-0.0012}$
Orbital inclination, i_C [deg.]	$\mathcal{U}(70.0, 90.0)$	$82.50^{+0.58}_{-0.53}$
Orbit semimajor axis, a_C [AU]	(derived)	$0.0720^{+0.0013}_{-0.0013}$
Relative orbital separation, a_C/R_\star	(derived)	$4.287^{+0.093}_{-0.085}$
Incident flux, $F_{inc,C}$ [$F_{inc,\oplus}$]	(derived)	$126.6^{+4.0}_{-2.6}$
<i>Star B</i>		
Stellar mass, M_B [M_\odot]	$\mathcal{T}(1.6, 0.1, 1.4, 1.8)$	$1.608^{+0.087}_{-0.088}$
Stellar radius, R_B [R_\odot]	$\mathcal{T}(3.5, 0.3, 2.5, 4.5)$	$3.61^{+0.11}_{-0.12}$
Limb darkening coefficient, u_1	$\mathcal{G}(0.592, 0.02)$	$0.569^{+0.019}_{-0.020}$
Limb darkening coefficient, u_2	$\mathcal{G}(0.141, 0.02)$	$0.131^{+0.020}_{-0.020}$
<i>Star C</i>		
Stellar mass, M_C [M_{Jup}]	$\mathcal{U}(0.0, 55000.0)$	$66.1^{+4.1}_{-3.2}$
Stellar radius, R_C [R_{Jup}]	$\mathcal{U}(0.0, 100.0)$	$1.524^{+0.070}_{-0.072}$
Eclipse depth, Δ_C [ppt]	(derived)	$1.880^{+0.089}_{-0.088}$
Eclipse duration, $T_{14,C}$ [hours]	(derived)	$8.873^{+0.071}_{-0.070}$
<i>Instrumental parameters</i>		
LC level	$\mathcal{U}(-500.0, 500.0)$	$58.9^{+6.7}_{-5.8}$
Dilution factor	$\mathcal{T}(0.28, 0.01, 0.2, 0.4)$	$0.2765^{+0.010}_{-0.0096}$
LC jitter [ppm]	$\mathcal{U}(0.0, 2000.0)$	$53.0^{+1.2}_{-1.1}$
δ_{HERMES} [km/s]	$\mathcal{U}(-40.0, 0.0)$	$-25.86^{+0.42}_{-0.41}$
σ_{HERMES} [km/s]	$\mathcal{U}(0.0, 2.1)$	$1.81^{+0.20}_{-0.24}$
δ_{CAFE2} [km/s]	$\mathcal{U}(-35.0, -10.0)$	$-23.63^{+0.18}_{-0.17}$
σ_{CAFE2} [km/s]	$\mathcal{U}(0.0, 2.0)$	$0.66^{+0.17}_{-0.12}$

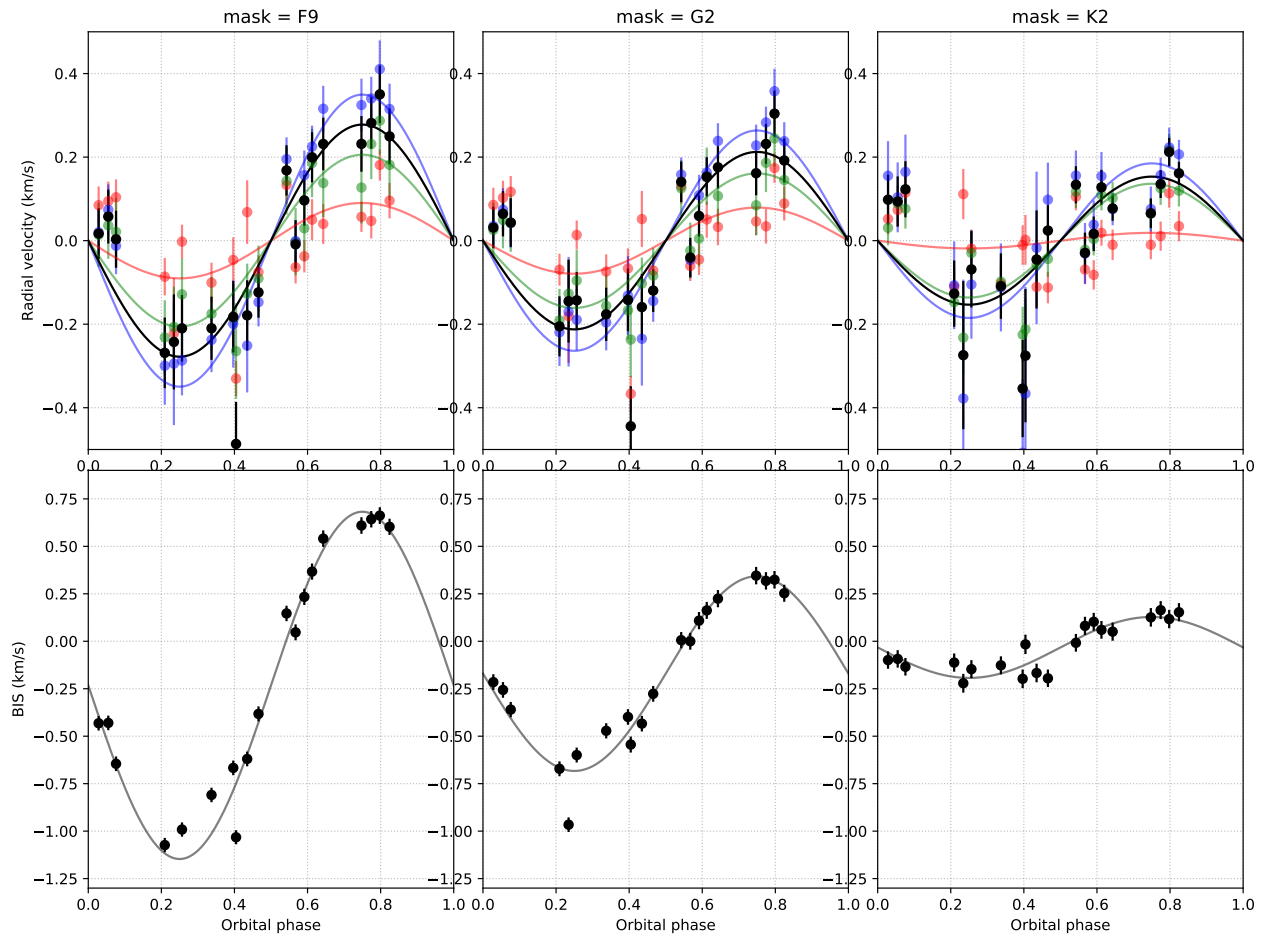


Fig. B.1. Inferred RV (top panels) and bisector span (bottom panels) for different binary masks (F9, G2, and K2 from left to right panels). In the top panels, the different colors show the RVs estimated with three different wavelength ranges: blue (3800Å-5100Å), green (5100Å-6400Å), and red (6400Å-7800Å). A simple maximum-likelihood model fit to the corresponding dataset is shown with solid lines. All panels are phase-folded with the *Kepler* eclipse periodicity.

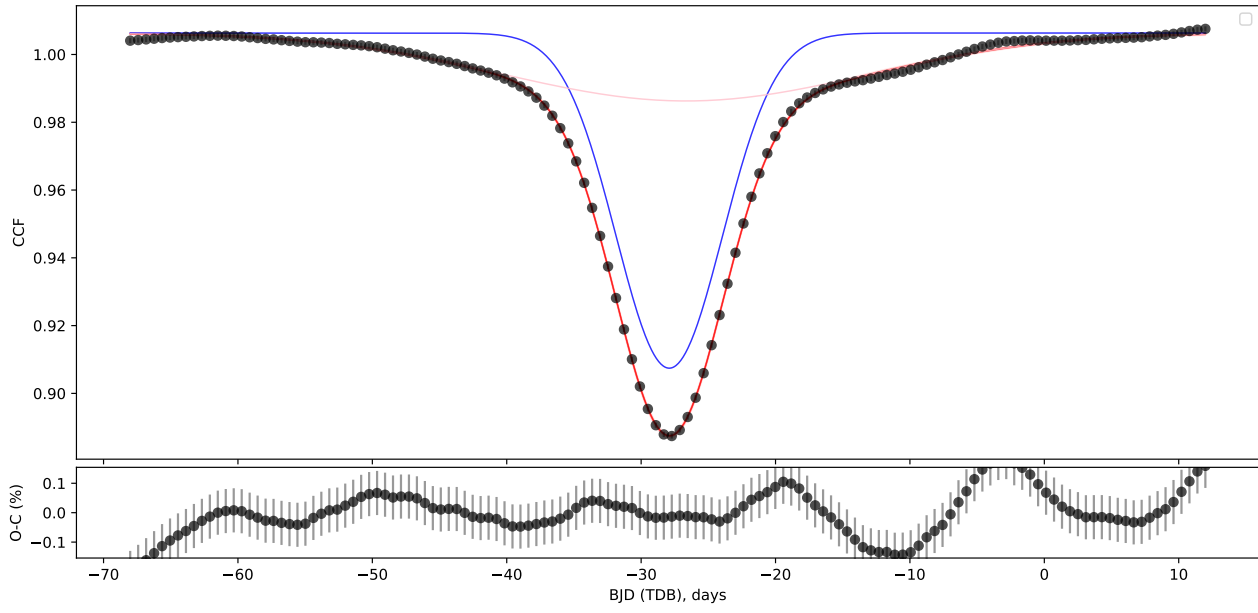


Fig. B.2. Example of the CCF of one of the HERMES spectra (black symbols). The two-component modeling of the CCF is shown as a red line, while the two individual components are shown in blue (sharp component, star A) and light pink (broad component, star B). The bottom panel shows the residuals after subtracting the two-component model to the CCF.

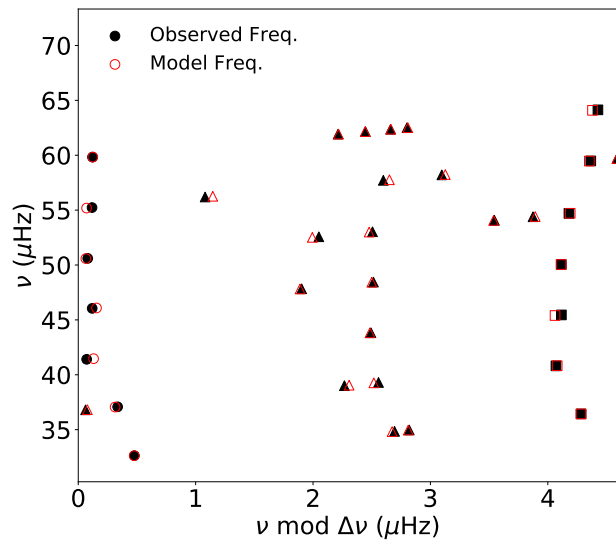


Fig. B.3. Échelle diagram representing the observed frequencies (filled black symbols) as well as the model frequencies (open red symbols) corresponding to a representative best-fitting model. No interpolation was used and so this corresponds to a specific model in the grid. The circles, triangles, and squares indicate the modes of angular degree $\ell = 0$ (radial modes), $\ell = 1$ (dipole modes), and $\ell = 2$ (quadrupole modes), respectively.

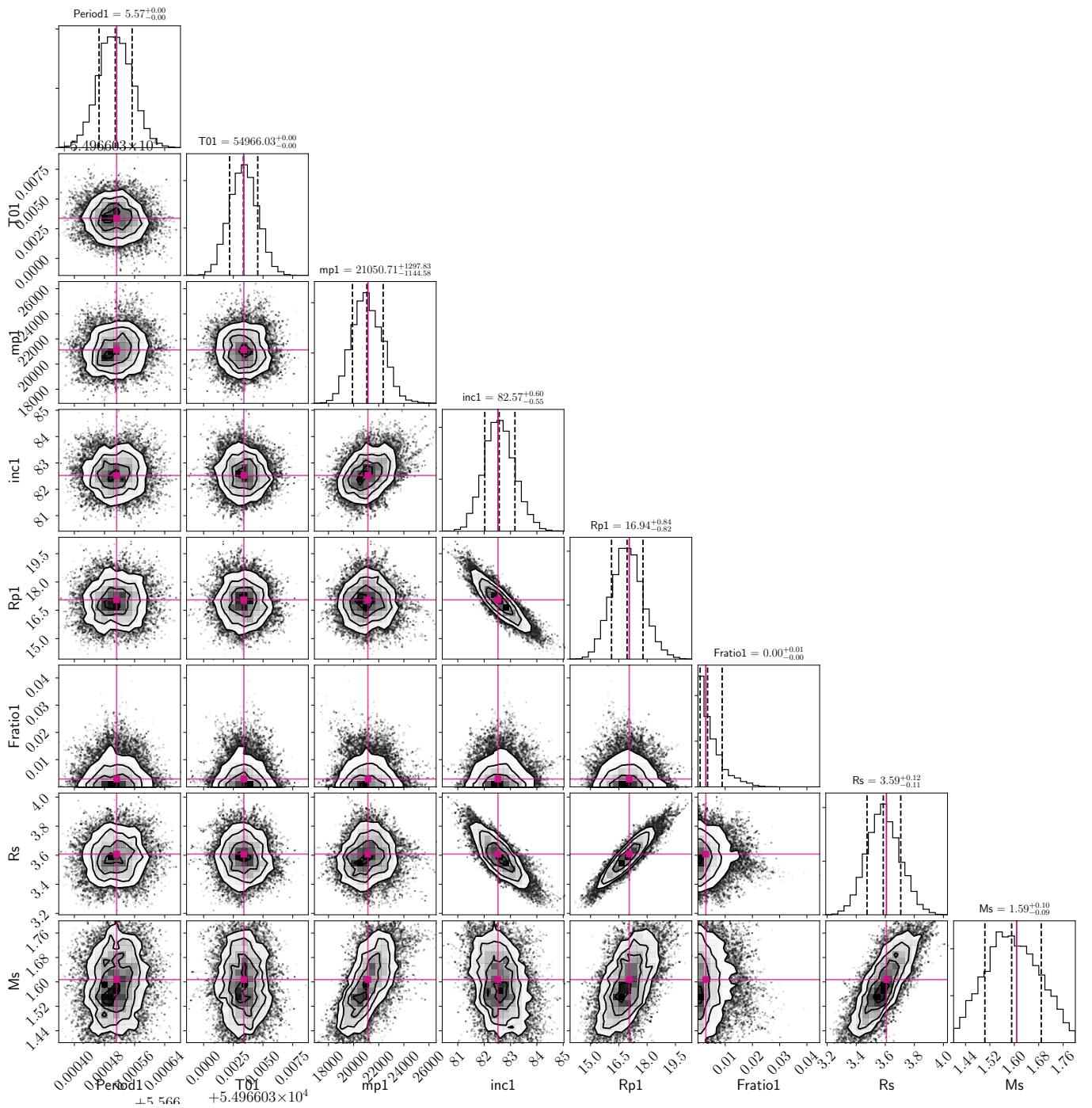


Fig. B.4. Corner plot of the joint light curve and RV analysis of the KOI-3886 system.